Mon. Not. R. Astron. Soc. **383,** 627–645 (2008) doi:10.1111/j.1365-2966.2007.12563.x

Photometric calibration of the *Swift* ultraviolet/optical telescope

T. S. Poole,[1] A. A. Breeveld,[1★] M. J. Page,[1] W. Landsman,[3] S. T. Holland,[3,4,5] P. Roming,[2] N. P. M. Kuin,[1] P. J. Brown,[2] C. Gronwall,[2] S. Hunsberger,[2] S. Koch,[2] K. O. Mason,[1,6] P. Schady,[1] D. Vanden Berk,[2] A. J. Blustin,[1] P. Boyd,[3] P. Broos,[2] M. Carter,[1] M. M. Chester,[2] A. Cucchiara,[2] B. Hancock,[1] H. Huckle,[1] S. Immler,[3] M. Ivanushkina,[2] T. Kennedy,[1] F. Marshall,[3] A. Morgan,[2] S. B. Pandey,[1] M. de Pasquale,[1] P. J. Smith[1] and M. Still[3]

[1]*Mullard Space Science Laboratory, University College London, Holmbury St Mary, Dorking, Surrey RH5 6NT*
[2]*Department of Astronomy & Astrophysics, Pennsylvania State University, 525 Davey Laboratory, University Park, PA 16802, USA*
[3]*NASA/Goddard Space Flight Center, Greenbelt, MD 20771, USA*
[4]*Universities Space Research Association 10211 Wincopin Circle, Suite 500, Columbia, MD 21044, USA*
[5]*Centre for Research and Exploration in Space Science and Technology NASA/Goddard Space Flight Center, Greenbelt, MD 20771, USA*
[6]*Science & technology Facilities Council, Polaris House, North Star Avenue, Swindon, Wilts SN2 1SZ*

Accepted 2007 October 9. Received 2007 October 9; in original form 2007 August 16

ABSTRACT

We present the photometric calibration of the *Swift* Ultraviolet/Optical Telescope (UVOT) which includes: optimum photometric and background apertures, effective area curves, colour transformations, conversion factors for count rates to flux and the photometric zero-points (which are accurate to better than 4 per cent) for each of the seven UVOT broad-band filters. The calibration was performed with observations of standard stars and standard star fields that represent a wide range of spectral star types. The calibration results include the position-dependent uniformity, and instrument response over the 1600–8000 Å operational range. Because the UVOT is a photon-counting instrument, we also discuss the effect of coincidence loss on the calibration results. We provide practical guidelines for using the calibration in UVOT data analysis. The results presented here supersede previous calibration results.

Key words: instrumentation: photometers – techniques: photometric – ultraviolet: general.

1 INTRODUCTION

The Ultraviolet/Optical Telescope (UVOT; Roming et al. 2005) is a modified Ritchey–Chrétien telescope with a 17 × 17-arcmin^2 field of view (FOV) operating in the 1600–8000 Å range. Like many optical telescopes, the UVOT uses broad-band filters in the ultraviolet (UV) and optical to obtain colour information. However, unlike most optical telescopes, the UVOT has a photon-counting detector that gathers data in a similar way to an X-ray detector.

The UVOT is one of three telescopes flying onboard the *Swift* spacecraft (Gehrels et al. 2004) and is co-aligned with the 15–150 keV Burst Alert Telescope (BAT; Barthelmy et al. 2005) and the 0.2–10 keV X-ray Telescope (XRT; Burrows et al. 2005). The primary goal of the *Swift* mission is to detect and characterize gamma-ray bursts (GRBs) and their afterglows. The design of the UVOT is well suited to this goal. In addition, UVOT's UV response in particular makes it a valuable instrument for other types of observations.

There are currently four near-UV imaging telescopes operating in space: *Hubble Space Telescope* (*HST*) – Wide-Field Planetary Camera 2 (WFPC2; Burrows et al. 1994), *XMM*-Optical Monitor (OM; Mason et al. 2001), *Galaxy Evolution Explorer* (*GALEX*; Siegmund et al. 2004; Milliard et al. 2001; Bianchi 2000) and *Swift* – UVOT. The *HST* has the highest spatial resolution and sensitivity but the smallest FOV. *GALEX* has the largest FOV and covers a larger UV wavelength range than OM or UVOT but it has very broad-band filters and the lowest spatial resolution of the four telescopes. The UVOT and OM are very similar in design, both covering approximately the same wavelength range and containing similar broad-band filters in both the UV and optical regimes. Both UVOT and OM include three UV filters that together cover approximately the same bandpass as the long-wavelength *GALEX* filter. The UVOT has a slightly broader point spread function (PSF) than OM but a higher sensitivity, by a factor of ∼10 at the bluest wavelengths. With respect to the four telescopes, UVOT, being mounted on *Swift*, is able to respond most quickly, making it the best instrument for observing transient phenomena.

In this paper, we describe the in-orbit photometric calibration of the UVOT and define the UVOT photometric system. We begin by

★E-mail: aab@mssl.ucl.ac.uk

© 2007 The Authors. Journal compilation © 2007 RAS

Table 1. *Swift*/UVOT filter characteristics. The central wavelength is the mid-point between the wavelengths at half-maximum.

Filter	Central wavelength (Å)	FWHM (Å)
v	5468	769
b	4392	975
u	3465	785
*uvw*1	2600	693
*uvm*2	2246	498
*uvw*2	1928	657

describing the UVOT technical details in Section 2, the calibration strategy in Section 3, followed by the observational measurements and photometry method in Sections 4–6. We review the calibration of the coincidence loss and position-dependent uniformity in Sections 7 and 8, respectively, and we provide the in-orbit effective area calculations, photometric zero-points, colour transformations and flux conversion factors in Sections 9–12. We test the calibration in Section 13 and give guidelines for making use of the calibration for UVOT data analysis in Section 14. Finally we summarize the calibration and discuss what is left to be done in Section 15.

Our preliminary UVOT calibration, described in Breeveld et al. (2005) and Ivanushkina et al. (2005), was released soon after launch in the HEASARC calibration data base (version 20050805 of the *Swift*/UVOTA CalDB).[1] Li et al. (2006) later gave an independent calibration for the optical filters using data from the earlier part of the mission. The calibration analysis described in this paper is the most detailed and comprehensive to date and thus supersedes our previous work.

2 UVOT TECHNICAL DETAILS

A technical description of the UVOT is given by Roming et al. (2005); we summarize the relevant properties here. The UVOT is of a modified Ritchey–Chrétien design, with a 30 cm primary mirror and an *f*-ratio of *f*/12.7 after the secondary. A 45° mirror directs photons into one of two detector units, one of which is kept in cold redundancy. Each detector unit consists of a filter wheel and microchannel plate intensified CCD (MIC; Fordham et al. 1992; Kawakami et al. 1994). The filter wheels contain 11 slots which house three optical filters, three UV filters, a clear *white light* filter (which transmits throughout the UVOT wavelength range of 1600–8000 Å), a magnifier, a low-resolution optical grism, a low-resolution UV grism and a blocked filter. The characteristics of the optical and UV filters can be found in Table 1.

The MIC detector has an entrance window that is slightly figured optically to flatten the image plane of the telescope. An S20 photocathode is deposited on the inside of the window and is optimized for the UV and blue wavelengths. The photocathode converts an incoming photon into an electron signal, which is then amplified by a factor of a million by a photomultiplier stage. Thus every incoming photon results in a cloud of electrons at the back of the photomultiplier, and these are converted back into photons by a phosphor screen. The resulting photon splash is recorded on a fast-scan CCD, which has an active area of 256 × 256 pixels. Each photon splash extends over several CCD pixels, and this allows the centroid of the splash to be determined in real time by fast onboard electronics to a fraction of a CCD pixel (1/8th of a CCD pixel in the case of the UVOT MIC detectors; Michel, Fordham & Kawakami 1997). The resulting image format is thus 2048 × 2048 pixels, covering an FOV of 17 × 17 arcmin^2. This provides a spatial sampling of 0.5 arcsec. There is a fibre taper between the phosphor screen and the CCD, which compensates for the larger physical area of the photomultiplier stage compared to the CCD. Throughout this paper, the word *pixel* refers to 0.5 × 0.5 arcsec^2 image pixels, unless explicitly stated otherwise.

The advantages of the MIC detector over a traditional 'bare' CCD are that (i) it is photon counting, (ii) it operates at 'room temperature' without the need for cooling and (iii) it is insensitive to cosmic ray and charged particle hits in the CCD. Because it is a photon-counting detector, the UVOT suffers from *coincidence losses* at high photon rates, when two or more photons arrive at a similar location on the detector within the same CCD readout interval (Fordham, Moorhead & Galbraith 2000). It is equivalent to 'pile-up' in an X-ray CCD detector. The magnitude of the effect depends on the readout rate of the CCD, which is once every 11.0329 ms when the full 256 × 256 CCD pixels are used, and faster when only part of the field is read out. In addition to coincidence loss the count rates also have to be corrected for the *dead time* while the charge is transferred out of the CCD, which amounts to 1.6 per cent of the full-frame readout interval. The loss due to dead time is a constant factor for a given readout rate, whereas coincidence loss also depends on the incoming photon rate.

For the full CCD, with a readout time of ∼11 ms, coincidence losses start to be significant at ∼10 counts s^{-1} and a correction should be applied to the recorded signal. Beyond ∼90 counts s^{-1}, equivalent to 1 count per frame, correcting for coincidence losses becomes increasingly uncertain. To extend the range of the detector to brighter sources, the readout rate can be increased, as noted above, by using only a subset of the CCD pixels. We use two pre-defined hardware windows, which are 120 × 120 CCD pixels (8 × 8 arcmin^2) and 75 × 75 CCD pixels (5 × 5 arcmin^2), centred on the observatory boresight. These reduce the frame times to 5.417 and 3.600 ms, respectively, and also reduce the dead time by a small amount.

The onboard algorithm that centroids the photon splash recorded on the MIC CCD uses a simple look-up table for speed. The intrinsic imperfections in this process mean that the subpixels within each physical CCD pixel do not all have the same effective physical area. The signature of this in the resulting image is an apparent 8 × 8 pixel fixed-pattern effect, sometimes referred to as 'mod-8 noise', though it is not strictly noise since photons are conserved (Michel et al. 1997). A calibration of this is derived onboard based on illuminating the field with an LED within the instrument, and applied as a correction to the centroiding algorithm. Nevertheless small gain variations over the face of the detector mean that a low-level residual fixed-pattern effect is still seen which varies in magnitude depending on position on the detector. If desired, the effect can be largely removed on the ground by using the tool uvotmodmap, which is released as part of the HEASOFT *Swift* FTOOLS software package.[2]

The UVOT operates in two data-taking modes: event and image. Event mode preserves the temporal and positional information of each photon. In image mode the photons are accumulated into an

[1] All the CalDB files can be found at http://swift.gsfc.nasa.gov/docs/heasarc/caldb/swift/.

[2] HEASOFT software can be found at http://heasarc.gsfc.nasa.gov/docs/software/lheasoft/.

image in the instrument's onboard memory before being telemetered to the ground, thus providing positional but not temporal information on the photons.

Because the spacecraft can drift slightly during an observation, the photon positions are shifted before they are added to memory. Occasionally, due to large spurious drifts in the spacecraft attitude information, individual frames are not added to the image. This time lost, when the onboard shift-and-add algorithm unnecessarily tosses events off the image, is known as TOSSLOSS. TOSSLOSS occurred fairly often until the software was fixed in 2005 September, but scarcely ever since then.

3 CALIBRATION STRATEGY

In the following sections we describe the different elements of the UVOT calibration in detail, but first we will outline the overall approach that we have taken. As a starting point, we used our ground-based measurements of the various components in the UVOT optical path, to produce an idealized or reference effective area curve for each of the UVOT filters. From these effective area curves, we predicted the count rates for a number of photometric standard stars for each of the UVOT filters. We then compared these predictions with in-orbit measurements of the standard stars to produce an in-orbit correction curve to the overall instrument response as a function of wavelength. Our predicted effective area curves were multiplied by the in-orbit correction curve to obtain the in-orbit effective area curves. Once the in-orbit effective areas were established, zero-points, colour transformations, flux conversion factors, etc. followed.

Any changes in the overall filter transmission are thus incorporated into the correction curve. Changes in filter transmission shape would be more difficult to deal with, but would show up as a difference in zero-point for sources of different colour. We do not find evidence for a change in the transmission shape for any of the filters.

4 UVOT INSTRUMENT RESPONSE

The instrument response of the UVOT is a product of:

(i) the telescope primary mirror geometric collecting area of 659 cm^2;

(ii) the mirror reflectivity (Roming 2007);

(iii) the filter transmission curves;

(iv) the detector quantum efficiency (DQE), which is the overall sensitivity of the photon-counting system, including the photocathode sensitivity (Kawakami 1999).

The DQE and filter transmission curves (for all but the *white* filter, see below) as a function of wavelength were measured in the laboratory at a subunit level. The mirror reflectivity was also determined in the laboratory, by measuring planar witness samples that were coated alongside the mirrors.

The measurements listed above, but not including the filter transmission curves, were combined to produce an idealized, or 'reference' response for the telescope, which is shown as a dashed line in Fig. 1. This is effectively the response expected if all the photons that pass through the telescope can be captured in the image. In practice, residual imperfections in the reflecting surfaces will scatter some photons into broad wings in the telescope PSF, and thus the actual throughput for photons in the image core will be less than ideal.

The dotted line in Fig. 1 is placed at the wavelength of 1600 Å, which is the short-wavelength limit of the instrument response determined by the detector window transmission. The long-wavelength cut-off has been set at 8000 Å. Outside the limits of 1600 and 8000 Å the DQE is very small; this range includes 99.98 per cent of the total instrument response.

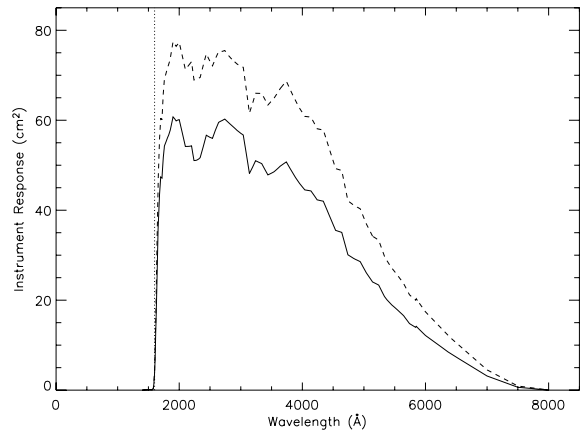

Figure 1. The instrument response of the UVOT including detector window, cathode sensitivity, mirror reflectivity and telescope area. The dashed line represents the idealized instrument response (assuming all photons are collected in the image) while the solid line shows the actual in-orbit response measured in a 5 arcsec radius circular aperture. The vertical dotted line marks the short-wavelength cut-off of the instrument at 1600 Å.

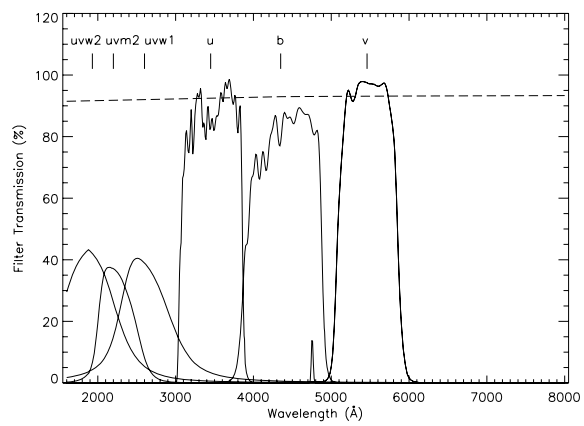

Figure 2. Filter transmission curves for the UVOT filters as measured in the laboratory. The *white* filter transmission curve is given by the dashed line; the identities of the other filters are indicated on the plot. The extra peak at ∼4750 Å is part of the *u* filter transmission.

Fig. 2 shows the transmission curves of the optical and UV filters as measured in the laboratory (Roming 2003). The extra peak at ∼4750 Å is part of the *u* filter transmission. The error at each point on these transmission curves is at most ±1 per cent (accounting for systematics), but is probably ±0.4 per cent. The curves provided for *uvw*2 do not extend shortward of 1800 Å due to the inability of the measuring device to provide data below this wavelength; therefore this filter curve had to be extrapolated to the 1600 Å limit assuming a peak at 1930 Å, and a symmetrical response profile. There were no laboratory measurements of the *white* light filter transmission as a function of wavelength. Instead, the curve that we have adopted, and which is shown in Fig. 2, is a model of the transmission, based on the design and substrate properties of the *white* filter.

The predicted effective area curves for each of the filters were obtained by combining the instrument response curve (Fig. 1) with the individual filter transmission curves (Fig. 2).

Table 2. Observational data used for the UVOT photometric calibration. The uses are given in column 4 where: OA is optimum photometric aperture (Section 6.1), BA is background aperture (Sections 6.2 and 6.3), CL is coincidence loss empirical correction (Section 7), PDU is position-dependent uniformity (Section 8), EA is in-orbit effective area curve (Section 9), ZP is photometric zero-points (Section 10) and CT is colour transformations (Section 11). The last three columns show the Johnson *V*, *B* and *U* magnitudes: for the Landolt sources from Landolt (1992), the Oke from Colina & Bohlin (1994) and white dwarfs calculated as described in Section 5.

Source	Date	Filter	Use	Origin	*V*	*B*	*U*
SA95−42	2005 July	*v*	EA, ZP, CT	Oke	15.606	15.391	–
g24−9	2005 July	*v*, *b*	EA, ZP, CF	Oke	15.751	16.176	–
WD1657+343	2005 February–April, June	*v*, *b*, *u*, *uvw*1, *uvm*2, *uvw*2, *white*	EA, ZP	White dwarf	16.4	16.2	15.0
WD1026+453	2005 July, October–November	*b*, *u*, *uvw*1, *uvm*2, *uvw*2	EA, ZP	White dwarf	16.1	15.9	14.8
WD1121+145	2005 February–May	*uvw*1, *uvm*2, *uvw*2, *white*	BA, EA, ZP	White dwarf	16.9	16.6	15.4
GD128	2005 November–December, 2006 January	*white*	OA, BA	White dwarf	15.89	15.82	–
Hz2	2005 November–December	*v*, *b*, *u*, *uvw*1, *uvm*2, *uvw*2	OA, BA	White dwarf	13.86	13.81	–
GD50	2005 December–2006 June	*v*	PDU	White dwarf	13.98	13.82	–
SA95−102	2005 March	*v*, *b*, *u*	EA, ZP, CT	Landolt	15.622	16.623	16.785
SA98−646	2005 March	*v*, *b*, *u*	EA, ZP	Landolt	15.839	16.899	18.325
SA101−278	2005 March, November	*v*, *b*, *u*, *white*	EA, ZP, CT	Landolt	15.494	16.535	17.272
SA101-13	2005 March, November	*v*, *b*, *u*, *white*	EA, ZP, CT	Landolt	15.953	16.590	16.557
SA104−244	2005 February–March	*v*, *b*, *u*, *white*	EA, ZP, CT	Landolt	16.011	16.601	16.449
SA104−338	2005 February–March	*v*, *b*, *u*, *white*	EA, ZP, CT	Landolt	16.059	16.650	16.568
SA104−367	2005 March–April	*v*, *b*, *u*	EA, ZP, CT	Landolt	15.844	16.483	16.357
SA104−443	2005 March–April	*v*, *b*, *u*	EA, ZP, CT	Landolt	15.372	16.703	17.983
SA104−457	2005 March–April	*v*, *b*, *u*	EA, ZP, CT	Landolt	16.048	16.801	17.323
PG1525−071b	2005 March	*v*, *b*, *u*	EA, ZP	Landolt	16.403	17.133	17.268
NGC 188	2005 October	*b*	CL	Open cluster	–	–	–
SA95	2005 July–October	*b*	CL	Star field	–	–	–
M67	2006 March	*b*	CL	Open cluster	–	–	–
SA104	2005 March	*b*	CL	Star field	–	–	–

5 STANDARD STAR DATA

Table 2 lists the standard stars and standard fields that were used for the calibration work presented in this paper. In total, two Oke standard stars, six white dwarf standards, ten Landolt standard stars, and four star fields have been used for the various calibration functions listed in Table 2.

For the standard stars used to determine the in-orbit effective areas, zero-points, colour transformations and count rate to flux conversion factors, our calibration procedure requires spectra that can be folded through the instrument response and filter transmission curves. It has been a challenge to find spectrophotometric standard stars, which are known to sufficient accuracy, have wide enough spectral coverage, are not variable and are not too bright for the sensitive UVOT detectors. Thus we have been limited in the UV to just three trusted white dwarf standards. For the optical we have used photometric standards to increase the sample of sources.

Representations of the Johnson *UBV* passbands are required for several aspects or our calibration (e.g. normalization of standard star spectra as described below and colour transformations from UVOT to the Johnson system). However, the true shapes of the Johnson *UBV* response curves have long been controversial (Bessel 2005). In this work, we have taken the following response curves to represent the Johnson *UBV* system. For the *V* and *B* responses we have used table 1, columns 'ϕ_V' and 'ϕ_B', respectively, from Ažusienis & Straižys (1969). For the Johnson *U* response, we have used table 2 from Buser (1978). Fig. 3 shows the comparison between the Johnson *U*, *B* and *V* and UVOT normalized *u*, *b* and *v* responses. In this paper we use the convention of capital letters for the Johnson system and lower case letters for the UVOT system.

For the two Oke standard stars, spectra were obtained from the ESO standard star archive (ftp://ftp.eso.org/pub/stecf/standards/hststan). These spectra cover the wavelength range 3200–8000 Å and are therefore only used to calibrate the *v* and *b* filters. As described in Colina & Bohlin (1994), the absolute photometric calibration of these spectra can be improved using precision ground-based photometry. These spectra were therefore folded through the Johnson *V* filter response and normalized to the *V* magnitudes given by Colina & Bohlin (1994).

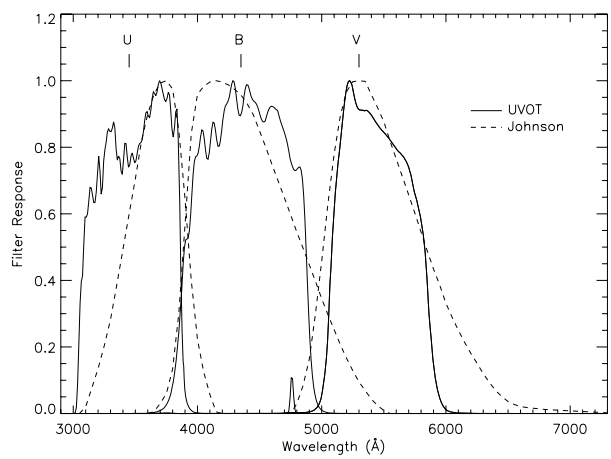

Figure 3. Comparison between the Johnson and UVOT optical responses. The Johnson responses are taken from Ažusienis & Straižys (1969) and Buser (1978), as described in Section 5.

Three of the white dwarf standards (WD1657+343, WD1026+453, WD1121+145) are used for the effective areas and zero-point calibration. Spectra were obtained from the

HST MAST archive (http://archive.stsci.edu/) of WD1657+343[3] and WD1026+453.[4] The spectrum of WD1026+453 had to be extrapolated longward of 5700 Å, and so this spectrum was not used for calibration of the v filter. For WD1121+145 we use the *IUE* spectrum presented by Holberg et al. (2003) and the optical spectrum from Massey et al. (1988). For these three sources, the Johnson magnitudes listed in Table 2 were obtained by folding their spectra through the Johnson *UBV* response curves.

The Landolt standard stars (Landolt 1992) do not have accurate spectra available in the literature. Therefore, the Landolt standard stars were matched to the stellar spectra from the catalogue of Pickles (1998) which had the closest $B - V$ and $U - B$ colours. The best matching Pickles spectra were then folded through the Johnson transmission curves and normalized to the U, B or V magnitudes from Landolt (1992) for calibration of the UVOT u, b and v filters, respectively.

5.1 In-orbit measurements

Table 2 gives observational details for all of the calibration sources and fields, including observation dates (column 2), the observed filters (column 3) and the photometric calibration product in which the source or field was used (column 4). Most of the observations were taken between launch and 2005 April, during the calibration phase of the *Swift* mission. For more details about the observational information please refer to the *Swift* Calibration Database (CalDB) documents[5] (Poole 2007a,b,c). The original ground-based *UBV* photometry for the Landolt standard stars was obtained using a 14 arcsec diameter aperture (Landolt 1992), which is not optimum for the UVOT calibration. We therefore checked each of the UVOT images of Landolt standard stars to ensure that there were no other stars of sufficient brightness to offset the photometric calibration, within 7 arcsec of the standard stars.

6 PHOTOMETRY METHOD

In this section we describe how and why we chose the photometric aperture and background region to use for the calibration analysis, and describe the analysis we undertook. We do not necessarily recommend following the same procedure for all UVOT data analysis and the reader is referred to Section 14 for more information on this.

Much of this analysis was performed using in-house IDL[6] routines which could be readily tailored to the calibration tasks at hand, and have allowed us to test analysis methods and calibration products that have subsequently been implemented in the official UVOT HEASOFT software and HEASARC calibration data base.

6.1 Optimum photometric aperture

One effect of coincidence loss (see Section 7) is that the shape of the PSF is slightly dependent on the source count rate. We wished to find an aperture enclosing the same percentage of the PSF regardless of count rate, if such an aperture existed. This was most easily found by using the same source and changing the frame rate to mimic a change in count rate and then looking for a consistent result after correcting for coincidence loss (see Section 7, equation 1). The use of different hardware window sizes, and hence frame times, allows coincidence loss to be varied without changing any other parameters. Therefore, we define the optimum photometric aperture radius to be that which gives rise to the smallest variation in the enclosed energy fraction for a point source as a function of coincidence loss. This is the most convenient aperture to use for the calibration because it gives consistent results for photometry over a wide range of count rates.

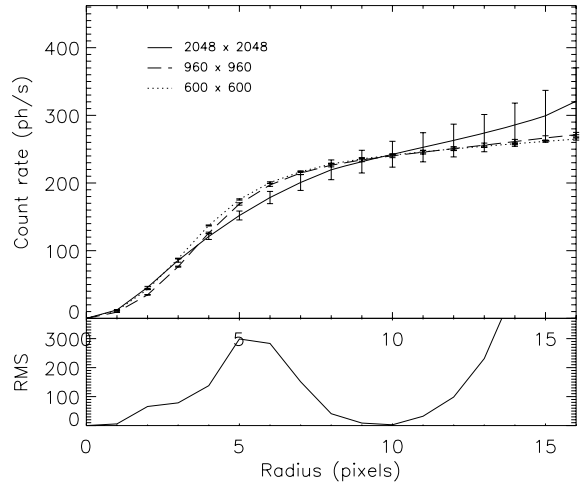

Figure 4. Coincidence-loss-corrected count rates within concentric radii, for Hz2 in the *uvw*2 filter, with a hardware window size of 2480 × 2480 (solid black line), 960 × 960 (dashed line) and 600 × 600 (dotted line). The error bars on the background-subtracted data were determined using Poisson statistics.

Table 3. Optimum aperture results obtained from Hz2 (optical and UV filters) and GD128 (*white* filter).

Filter	Aperture radius (pixels)	Range (pixels)
v	11.7	2.6
b	10.8	1.2
u	8.7	1.8
*uvw*1	12.5	0.9
*uvm*2	10.0	0.5
*uvw*2	9.7	0.3
white	9.8	1.3

The optimum aperture was investigated using observations of two isolated, bright stars GD128 and Hz2, for the default set of hardware windows with sides of length 2048, 960 and 600 pixels. Hz2 was used for the optical and UV filters, but is too bright for the *white* filter, for which GD128 was used. The raw count rates were corrected using the theoretical coincidence loss equation only (see Section 7, equation 1), which takes the frame time into consideration. Fig. 4 shows an example of this for the *uvw*2 filter. The minimum of the rms curve coincides with the optimum aperture radius.

Table 3 shows the results from Hz2 (optical and UV filters) and GD128 (*white* filter) for the optimum aperture: the optical, UV and *white* filters have optimum aperture radii of 10.1 ± 1.3, 10.7 ± 1.5 and 9.8 ± 1.3 pixels, respectively. Since these are similar, and consistent within the uncertainties with a mean of 10.5 ± 1.2 pixels, we chose to use a radius of 10 pixels (5 arcsec) for all the photometric calibration analysis.

The percentage of counts within the chosen 10 pixel aperture radius is stable for moderate count rates. Assuming that a 55 pixel

[3] MAST IDs: 08v101010, 08h111010, 08h111040, 08v101030.
[4] MAST IDs: 08h106040, 08h106010, 08h106020.
[5] http://swift.gsfc.nasa.gov/docs/heasarc/caldb/swift/.
[6] From ITT Visual Information Solutions.

© 2007 The Authors. Journal compilation © 2007 RAS, MNRAS **383,** 627–645

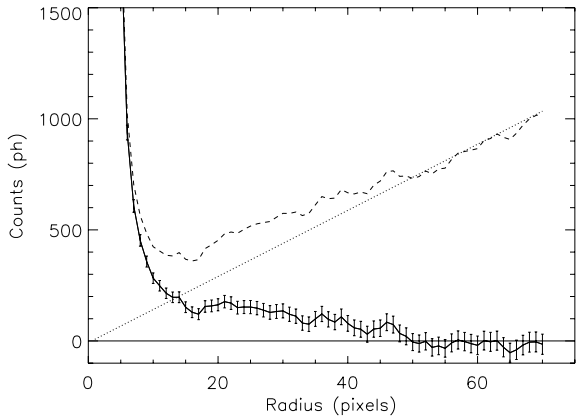

Figure 5. Data for Hz2 in the *b* filter with a hardware window size of 960 × 960. The dashed line represents the number of counts in each consecutive ring for the source plus background measurements, the dotted line is the number of counts in each consecutive ring for the background only, and the solid black line is the number of counts in the rings once the background has been subtracted. The error bars on the background-subtracted data are due to Poisson statistics.

radius aperture represents 100 per cent of the PSF (see Section 6.3 and Breeveld et al., in preparation), then 85.8 ± 3.8 per cent of the PSF is contained within the 10 pixel radius for all filters including the *white* filter. The differences between the enclosed energy fraction within our adopted 10 pixel radius aperture, and the optimum apertures we determined for the individual filters (Table 3) are very small because this radius is already in the wings of the PSF where the count rates are low (Fig. 5). In the case of *uvw*1, which has the largest difference between the optimum aperture radius of 12.5 pixels, and our adopted aperture radius of 10 pixels, the difference in the enclosed energy fraction is at most 2 per cent.

6.2 Subtracting the background

Two methods of determining the background count rate were considered: mean background, or clipped-mean background. The mean background method averages the number of counts per pixel over the background aperture, whereas the clipped-mean background method excludes any background pixels with count rates more than 3σ above the initial mean and then averages the counts over the remaining background aperture pixels. The advantage of the clipped-mean background method is that it removes counts from any significant sources that may lie within the background aperture. However, the disadvantage is that it produces a consistently lower value because it removes the top of the distribution, which is assumed to be Gaussian. For very low rate backgrounds, as is often the case with UVOT, this assumption is not valid: most pixels contain either 1 or 0 counts.

Using the software package GAIA (starlink GAIA version 2.8-0) the clipped-mean method was consistently smaller than the mean method by 0.14 ± 0.03 photons pixel^{-1}. An in-house IDL routine was also used, and also resulted in a consistently lower background value when using the clipped-mean method. This is acceptable when observations have high backgrounds, but will have a significant effect on count rates for observations with lower backgrounds and faint sources. Hence, a background limit of 10 photons pixel^{-1} was set (where the measured background difference is 1.4 per cent of the total background), above which the clipped-mean background method is applied, and below which the simple mean background method is used unless there is an obvious source that lies within the background region.

Table 4. Radius at which the count rate per pixel of the source becomes indistinguishable from the background.

Filter	Hz2 (pixels)	GD128 (pixels)	WD1121+145 (pixels)
v	20	–	15
b	50	–	15
u	51	–	21
*uvw*1	52	–	45
*uvm*2	54	–	52
*uvw*2	55	–	48
white	–	30	20

6.3 Background region size

For bright sources PSF wings can be seen that extend out to around 40–55 pixels. Investigation into the extent of the PSF wings was carried out by examining images of three white dwarf standard stars (Hz2, GD128 and WD1121+145) of different magnitudes, with the three default hardware window sizes.

For each case we measured the total number of source and background counts in 70 concentric rings around the source; each ring one pixel wide and varying in radius from 1–70 pixels from the centre of the source. An example is shown in Fig. 5. The background-subtracted source counts are represented by the solid black line, and in this example the radius at which the total number of counts becomes indistinguishable from the background, is at around 50 pixels radius. Table 4 shows the radius at which the count rate per pixel of the source becomes indistinguishable from the background. These results show that even in the case of the faint source, WD1121+145, very faint PSF wings are still sometimes observed.

From these results the background region should be at least 55 pixels from the centre of the source, thereby avoiding any PSF wing photons in the background calculations. We used an annulus with inner radius 55 pixels from the centre of the source and an outer radius of 70 pixels to produce a large sample of background area with which to calculate the background contribution.

6.4 Count rate calculations

The method used to obtain corrected count rates for standard star UVOT calibration observations is outlined in the following section. This is the procedure that was used for the calibration analysis, and is not necessarily a recipe for analysing GRB data. Please go to Section 14 for practical guidelines to analysing data.

The raw image data from the UVOT was pre-processed using the standard *Swift* pipeline (UVOT2FITS v3.16). The first step of the pipeline is to construct a bad pixel map for each exposure and then to use this map to exclude pixels from further analysis. Next, fk5 equatorial coordinates were applied to each exposure and the exposures were rotated so that north is up and east to the left-hand side. This coordinate system is applied using information from the *Swift* star trackers, which are accurate to 5 arcsec. The pipeline corrects for this uncertainty by matching the star field in each exposure to sources in the *HST* Guide Star Catalogue. This aspect correction is accurate to 0.5 arcsec (90 per cent confidence radius). The radial aperture size of 10 pixels meant that a fixed pattern correction (see Section 2) did not need to be applied to these data.

Following is a list of steps taken to determine the count rates of standard stars from the sky images produced by the *Swift* pipeline.

(i) We obtained an aspect-corrected image in SKY coordinates from the *Swift* archive (http://swift.nasa.gov/docs/swift/archive).

(ii) We removed any exposures or observations that contained any exposure time anomalies.[7]

(iii) Where multiple exposures were taken in an observation, count rates were calculated for the individual exposures, and then a weighted mean obtained.

(iv) We obtained observed (source + background) counts using a 10 pixel (5 arcsec) radius aperture.

(v) We obtained the dead time corrected exposure time for each exposure to calculate the count rate (the EXPOSURE keyword in the UVOT sky image files).

(vi) We obtained the background count rate from an annulus with an inner radius of 55 pixels and an outer radius of 70 pixels centred on the source. If the background level was below 10 photons pixel^{-1} we used a mean background method, or if it was above this level we used a clipped-mean background method, as described in Section 6.2.

(vii) We corrected the (source + background) and background count rates for coincidence loss using equation (3), as described in Section 7.

(viii) Finally, we subtracted the coincidence-loss-corrected background count rate from the coincidence-loss-corrected (source + background) count rate to obtain the coincidence-loss-corrected source count rate.

Errors on the count rates were calculated using Poisson statistics and were carried through the coincidence loss equations to produce final coincidence-loss-corrected count rate errors.

7 COINCIDENCE LOSS

As described in Section 2, the UVOT detector suffers from coincidence losses at high count rate when multiple photons arrive at the same location on the detector during a single frame (see Fig. 6). The theoretical coincidence-loss-corrected count rate for a single-pixel detector is

$$C_{\text{theory}} = \frac{-\ln(1-\alpha C_{\text{raw}} f_t)}{\alpha f_t}, \tag{1}$$

where C_{theory} is the incident count rate (in counts s^{-1}) and C_{raw} is the raw observed count rate (also in counts s^{-1}) calculated using the *dead time corrected* exposure time (keyword EXPOSURE in the UVOT image FITS file header). f_t is the frame time (0.011 0329 s for a full frame; keyword FRAMTIME in the FITS file header) and α is the dead time correction factor (1 minus the dead time fraction; 0.9842 for a full frame; keyword DEADC in the FITS file header).

This theoretical coincidence loss expression cannot be applied on a pixel-by-pixel basis to UVOT images because each count assigned to a UVOT pixel is determined by centroiding a photon splash over five physical CCD pixels (in a 'cross-hair' sampling). The effect of high coincidence loss is thus not only to lose counts, but also to reposition counts, since overlapping photon splashes within a single frame will be misplaced by the centroiding algorithm.

We therefore introduce an empirical polynomial correction to account for the differences between the observed and theoretical coincidence loss correction:

$$f(x) = 1 + a_1 x + a_2 x^2 + a_3 x^3 + a_4 x^4, \tag{2}$$

where $x = C_{\text{raw}} f_t$. Hence we have a full coincidence loss corrected incident count rate of

$$C_{\text{corr}} = C_{\text{theory}} f(x), \tag{3}$$

where C_{corr} and C_{theory} are both in counts s^{-1}. The coefficients in equation (2) were determined by a least-squares fit to minimize the differences between the UVOT b magnitudes of 361 isolated stars in the open cluster NGC 188, with the catalogue of Stetson, McClure & VandenBerg (2004). The count rates were measured within 10 pixels as described in Section 6.4. The fit yielded the values $a_1 = 0.066$, $a_2 = -0.091$, $a_3 = 0.029$ and $a_4 = 0.031$. Fig. 7 compares the UVOT and Stetson photometry of the 361 stars in NGC 188 after the polynomial correction has been applied to the

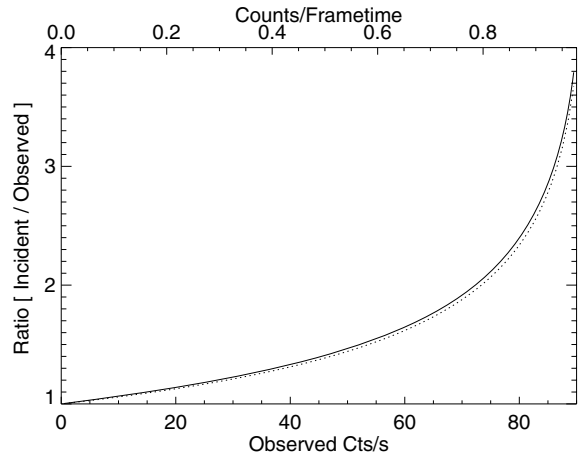

Figure 6. The size of the coincidence loss correction (the ratio of the incident to observed counts) is shown as a function of the observed dead time corrected count rate for the nominal full-frame observing mode. The dotted line shows the expected relation for a single pixel device, while the solid line includes our empirical polynomial adjustment to the theoretical relation. The top axis shows the number of counts per frame.

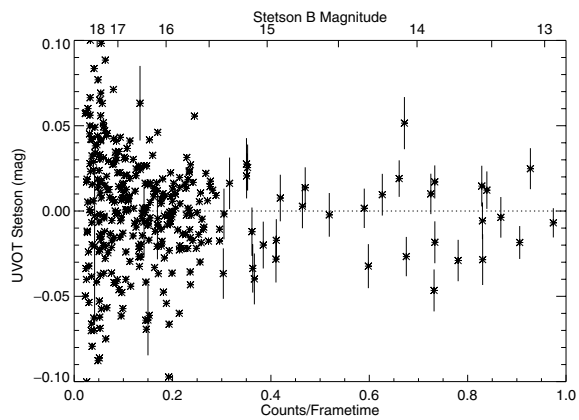

Figure 7. The difference between UVOT and Stetson et al. (2004) magnitudes for 361 isolated stars in the open cluster NGC 188 is plotted against the number of counts per frame (bottom x-axis) and Stetson B magnitude (top x-axis). A polynomial correction has been applied to the theoretical coincidence loss curve for UVOT to minimize any systematic trend with the Stetson magnitudes. For clarity, only selected Poisson error bars are included for counts per frame time of less than 0.3.

[7] Please see http://heasarc.gsfc.nasa.gov/docs/swift/analysis/uvot_digest.html for more details on timing problems.

UVOT data. This correction was verified using UVOT observations of other photometric fields (SA95, M67, SA104) also studied by Stetson (2000). Note that the polynomial component changes the coincidence loss correction by less than 3 per cent for count rates up to 0.96 counts per frame (87 counts s^{-1} for a full frame), at which point the coincidence loss correction is a factor of 3.4.

The coincidence loss correction here applies to isolated point sources and does not apply for crowded or extended sources, or when a smaller aperture is needed to maximize the signal-to-noise ratio. There is no general solution to these problems though we note that for faint sources, it may be preferable to maximize the signal-to-noise ratio with a small aperture, and accept some increased scatter in the small coincidence loss correction (see Section 14).

The finite number of frames in an exposure implies that the measured count rate follows a Binomial distribution. Because of this, normal photometry packages which assume Poisson statistics will not give an accurate measure of the error, except at low count rates. Since the incident count rate must be derived by use of the non-linear coincidence loss correction according to equation (1), the error in the incident count rate, σ_{theory}, is given by (see Kuin & Rosen 2007)

$$\sigma^{\pm}_{\text{theory}} = -\frac{1}{\alpha f_t} \ln\left(1 \pm \frac{\sigma_{\text{raw}} f_t}{1 - C_{\text{raw}} f_t}\right), \tag{4}$$

where σ_{theory} is in counts s^{-1}, and $\sigma_{\text{raw}} = \sqrt{C_{\text{raw}}(1 - C_{\text{raw}} f_t)/t_{\text{elapsed}}}$ (in counts s^{-1}) is the binomial error in the measured count rate. For low count rates, the Poisson error is therefore a good approximation. For the highest incoming photon fluxes (more than 0.9 counts per frame) the upper error becomes larger than the lower error, but in most cases of interest, they are nearly equal.

Based on the NGC 188 photometry, any additional systematic error introduced by the coincidence loss correction is less than 0.01 mag. This is confirmed in the comparison data sets where no trend is seen with magnitude.

8 POSITION-DEPENDENT UNIFORMITY

The photometric sources were all measured near the middle of the detector, but any variation in sensitivity from position to position due to irregularities in the fibre bundle, photocathode, etc., or any larger scale trend in sensitivity over the FOV clearly should be taken into account.

Large-scale sensitivity (LSS) variations over the area of the detector were measured using the count rate of a standard star at a variety of positions on the detector. For this we used GD50, and several other stable stars to evenly sample the whole FOV, giving 163 points in total. The standard deviation of the normalized count rate of all these points is 3.2 per cent, but for the central 1024 × 1024 region only, the standard deviation is 2.0 per cent. A trend of count rate versus position could clearly be seen, so the data were binned spatially into 16 bins, with a minimum of four measurements per bin, to remove small-scale variations. The LSS variation over the full FOV demonstrated by the binned data has a 2.2 per cent standard deviation with a peak to trough range of 8 per cent. Fig. 8 is a shaded plot showing this variation. One corner has a higher sensitivity and the opposite corner lower. However, after binning, the central region of the detector (the central 1024 × 1024 pixels, equivalent to the middle four boxes in the diagram) within which the photometry measurements were taken appears to have more-or-less flat sensitivity showing a standard deviation of 0.6 per cent.

An upper limit to the small scale, or pixel-to-pixel sensitivity variation, is found from repeated measurements of the same object

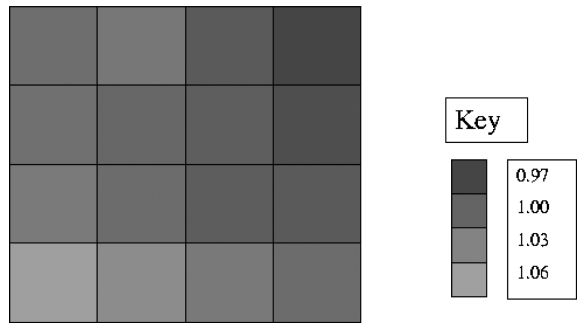

Figure 8. Shaded plot showing how the sensitivity of the UVOT varies with position. The paler areas are more sensitive. The data are binned to make 4 × 4 bins with a minimum of 4 points per bin.

(GD50) at slightly different positions in the central area and is found to be at most 2.3 per cent standard deviation. This has been confirmed by the measurements of several stars used in the long-term stability calibration, and also by the pixel-to-pixel variations in count rate in exposures taken with the onboard LED. At present, it would be prudent to assume a 2.3 per cent systematic error on individual UVOT photometry measurements.

A more detailed analysis of large- and small-scale sensitivity and of the sensitivity changes over the lifetime of UVOT will be presented in a future paper (Breeveld et al., in preparation).

9 IN-ORBIT EFFECTIVE AREA DETERMINATION

The predicted effective area curves for each filter were calculated in units of cm^2 by multiplying the UVOT reference instrument response (Fig. 1) by the ground-based filter transmission curves (Fig. 2). This section describes how the curves were adjusted to produce the in-orbit effective area curves.

9.1 In-orbit instrument response curve

To obtain in-orbit effective area curves, the instrument response curve was adjusted using an in-orbit correction curve. The correction curve was produced using the standard star observations through the UV and optical filters. For each star, in each filter, the ratio of the observed count rate to the predicted count rate was computed. These ratios were averaged for all the stars in each filter. These average in-orbit/predicted ratios and their corresponding standard errors can be seen in Table 5.

The correction curve was produced by fixing the ratio values at the central wavelengths of each filter (Table 1), and applying a spline fit. The correction curve was assumed to be constant longwards of the central wavelength of the *v* filter and shortwards of the central

Table 5. Ratio of observed to predicted count rates used to produce an in-orbit correction curve.

Filter	Average count rate ratio	Standard error	Number of observations
v	0.698	0.008	13
b	0.725	0.011	12
u	0.753	0.014	11
*uvw*1	0.786	0.009	3
*uvm*2	0.740	0.010	3
*uvw*2	0.784	0.009	3

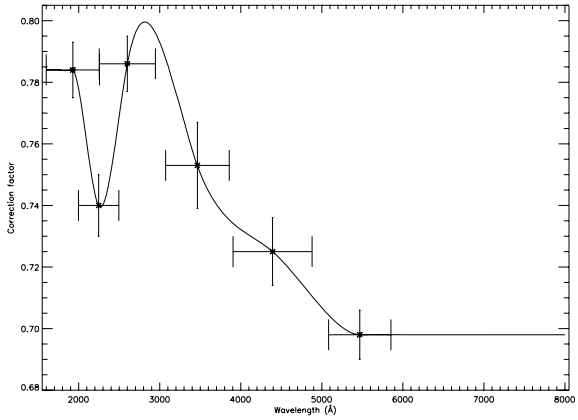

Figure 9. In-orbit correction curve made by a spline fit to the ratios given in Table 5. The *y*-axis error bars show the standard error for each ratio; the *x*-axis error bars show the FWHM of each filter (Table 1).

wavelength of the *uvw*2 filter. Fig. 9 shows the in-orbit correction curve. The shape of this curve, which represents the deviation from the ideal response, is not consistent with significant contamination of the optical surfaces by molecular material, which would have a greater effect in the UV than in the optical. This in-orbit correction curve was then multiplied by the reference instrument response curve to produce the in-orbit instrument response curve shown as the solid black line in Fig. 1.

9.2 In-orbit effective area curves

The in-orbit effective area curve for each filter, except for *white*, was calculated by multiplying the in-orbit instrument response with the ground-based filter transmission curves. Fig. 10 shows the resulting in-orbit effective area curves.

The *white* filter is a special case because it covers a very wide band, and so the shape of its effective area curve depends on the shape of the instrument response curve throughout the wavelength range. Unfortunately, it is also the one filter that does not have a well-measured throughput, and so a different sequence was followed for the calibration of the *white* filter effective area. First, we combined the *white* filter predicted transmission curve with the in-orbit instrument response function to predict the count rates of the standard stars observed through this filter. We then compared these with the observed count rates, to find the average in-orbit correction factor for the *white* filter. This ratio was found to be 0.88 ± 0.05. Unlike the other optical and UV filters, the *white* filter in-orbit effective area curve was then calculated by combining the in-orbit instrument response curve with the theoretical *white* filter transmission curve and then multiplying by the extra factor of 0.88.

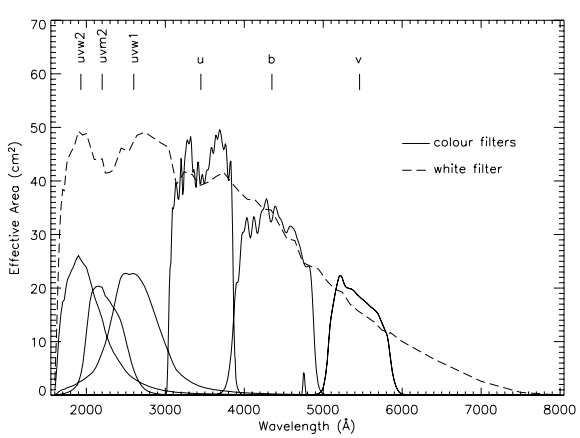

Figure 10. In-orbit effective area curves for the UVOT filters.

10 PHOTOMETRIC ZERO-POINTS

The photometric zero-point $Z_{\rm pt}$ of each UVOT filter is defined as the magnitude which is equivalent to 1 count s^{-1} (Pogson 1856), and is given by the equation

$$Z_{\rm pt} = m_{\rm source} + 2.5 \log (C_{\rm source}) , \tag{5}$$

where $m_{\rm source}$ is the magnitude of a source, and $C_{\rm source}$ is the count rate of an observed source after correction for coincidence loss and dead time.

We have taken the observed spectrum of Vega from Bohlin & Gilliland (2004) to define our UVOT magnitude system. Thus this spectrum of Vega represents $m_{\rm Vega} = 0$ in all filters. Transformations are provided in Section 11 to convert from the UVOT system to the Johnson system. The zero-points for the optical and UV filters were calculated by standardizing the count rates to the Vega spectrum. The expected count rate of each observed star [$C_{\rm exp}(i)$] was calculated by folding its spectrum through the in-orbit filter effective areas (Section 9.2). In the same way the spectrum of Vega was used to produce an expected Vega count rate [$C_{\rm exp}$(Vega)]. The zero-points [$Z_{\rm pt}(i)$] for each source in each filter were then calculated using

$$Z_{\rm pt}(i) = m_{\rm Vega} + 2.5 \log \left[C_{\rm exp}({\rm Vega}) \frac{C_{\rm obs}(i)}{C_{\rm exp}(i)} \right] . \tag{6}$$

The final zero-point ($Z_{\rm pt}$) for each filter was calculated by averaging over all the observations in that filter.

Fig. 11 shows the data used to produce the zero-points for each of the UVOT filters. The final, mean zero-point is shown with a dashed line, and the rms scatter is illustrated with dotted lines to either side. The error bars shown on the individual points in the plots include the Poisson error in the raw observed count rate, and the errors associated with the stellar spectra used. The predicted errors on the Landolt stars in the optical filters were calculated using an estimate of the systematic error between the Landolt and Johnson system (Menzies et al. 1991) added in quadrature with the Landolt colour term errors (Landolt 1992). The predicted errors on the Landolt stars in the *white* filter were calculated to be 4 per cent due to the scatter of possible Pickles spectral matches and this was added in quadrature with the Landolt colour term errors (Landolt 1992). The Oke and *white* dwarf predicted errors in all filters were calculated using a *HST* spectrophotometric error of 2 per cent (Bohlin 2007) or an *IUE* error of 3 per cent (Massa & Fitzpatrick 2000).

Table 6 shows the final zero-points. For each filter the average error, which is the mean of the individual errors for each point, is given in column 6. As expected, this average error is comparable to the rms scatter about the mean, which is given in column 5. The error shown in column 4 is the standard error for each zero-point, which is a measure of the error on the mean and is smaller than the rms. However, the standard errors for the UV zero-points are based on only three data points in each filter, and the standard error for the *white* zero-point is based on only six data points, so these cannot be considered as valid estimates of the uncertainties on the zero-points. For this reason, for the UV and *white* zero-points, we recommend using the errors from column 6 in Table 6 as the uncertainties on

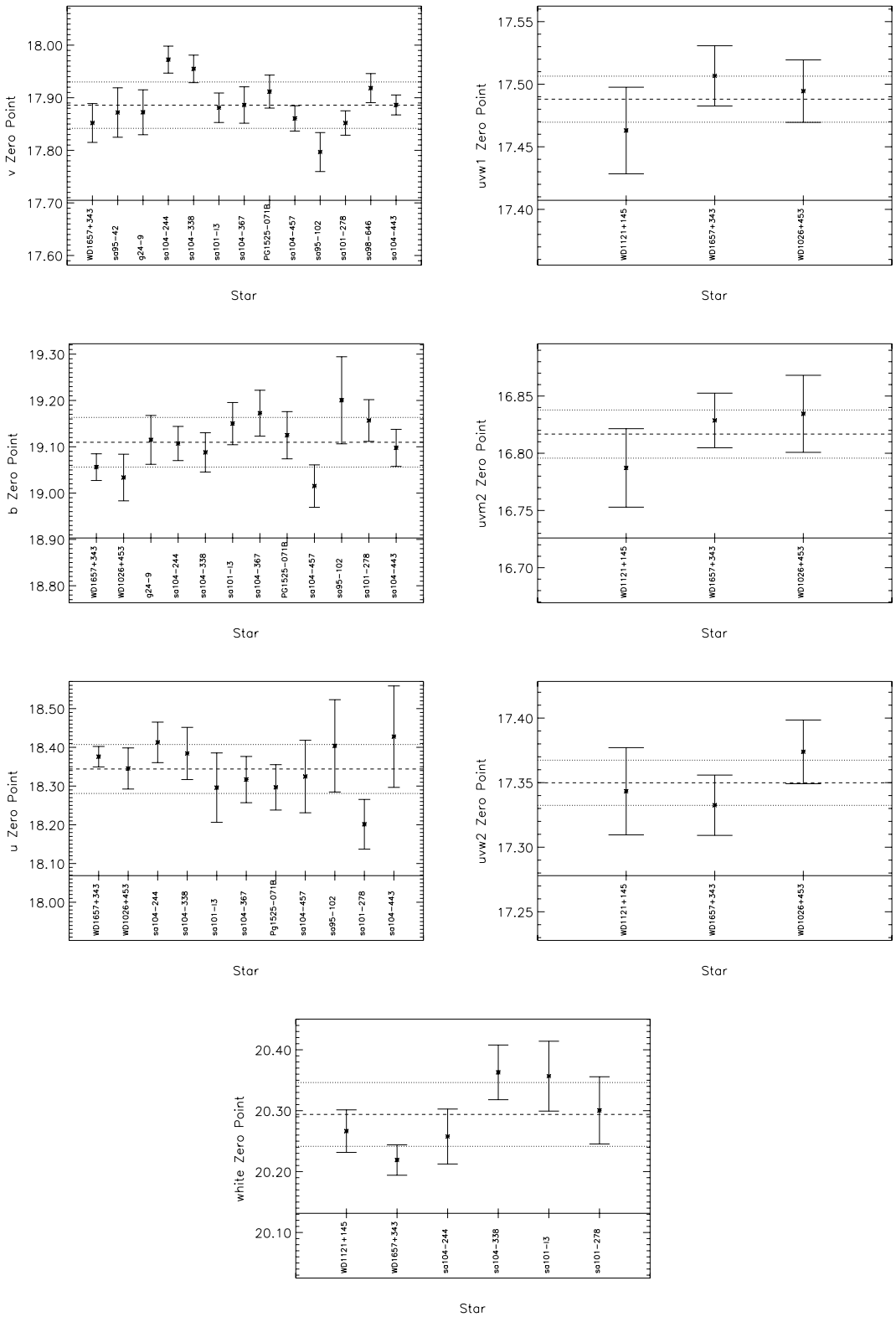

Figure 11. Zero-point calculations for the UVOT filters. Left-hand column: v, b and u filters; right-hand column: $uvw1$, $uvm2$ and $uvw2$ filters; bottom: *white* filter. Each point represents the zero-point obtained from a single standard star, labelled individually on the x-axis. The error bars include the Poisson error in the raw observed count rate and the errors associated with the stellar spectra used (see Section 10). The dashed line indicates the mean zero-point, with the dotted lines showing the 1σ rms error.

Table 6. In-orbit zero-points. The standard error (column 4) is the error on the mean zero-point for each filter; the rms (column 5) gives the scatter; the average error (column 6) includes uncertainties on individual measurements. Column 3 (recommended uncertainty) lists the recommended error for each zero-point.

Filter	Zero-point	Recommended uncertainty	Standard error	rms	Average error
v	17.89	0.013	0.013	0.04	0.03
b	19.11	0.016	0.016	0.05	0.05
u	18.34	0.020	0.020	0.06	0.07
*uvw*1	17.49	0.03	0.013	0.02	0.03
*uvm*2	16.82	0.03	0.015	0.02	0.03
*uvw*2	17.35	0.03	0.012	0.02	0.03
white	20.29	0.04	0.023	0.05	0.04

the zero-points. For the convenience of the reader we have listed the recommended zero-point error for all filters in column 3.

11 COLOUR TRANSFORMATIONS

Colour transformations are needed to convert from the UVOT magnitude system to any other system, in order to compare UVOT data with photometry from other sources. In this section we provide colour transformations to convert from the UVOT system to the Johnson system for a range of stellar spectra. We also provide transformations for a set of synthetic GRB spectra because *Swift* is primarily a GRB mission.

The colour transforms from the UVOT *ubv* system to the Johnson *UBV* system were calculated for stars using Pickles spectra (Pickles 1998), and for GRB model spectra. The model GRB spectra were generated assuming a power-law continuum and varying degrees of dust extinction, with the form $F_\nu^{-\beta}\exp^{-\varepsilon}$, where β is the GRB spectral index, and $\varepsilon = A_\lambda/A_v$ is the relative extinction per unit wavelength. The wavelength dependence of the extinction was modelled on the Small Magellanic Cloud extinction law (Pei 1992), and GRB spectra were produced for $\beta = 0, 1, 2$, rest-frame visual extinctions $A_v = 0.0, 0.2, 0.4, 0.8, 1.0$ mag and redshift in the range $0.3 < z < 2.0$.

To produce the Johnson colours and magnitudes, the Pickles spectra and GRB models were folded through the Johnson response curves (described in Section 5). To produce the UVOT colours and magnitudes the same spectral models were folded through the UVOT in-orbit effective areas to produce expected UVOT count rates ($C_{\rm source}$), then converted into magnitudes using

$$m_{\rm source} = Z_{\rm pt} - 2.5\log(C_{\rm source}), \tag{7}$$

where $m_{\rm source}$ is the magnitude of the source in the UVOT system, and $Z_{\rm pt}$ is the zero-point of each filter (listed in Table 6).

Fig. 12 plots the difference between UVOT and Johnson colours against UVOT colours for the optical filter combinations. The stars in each plot represent the Pickles stars, and the triangles represent the GRB models. The solid line in each plot shows the second-order polynomial fit for Pickles stars; the dotted line shows the second-order polynomial fit for the GRB models, and the dashed line shows where the colours in the two systems would be equal. The rms error on the residuals, and the ranges for which the fits have been calculated, can be seen in Table 7. The colour terms in these Pickles star polynomial fits are

$$\begin{aligned} U - B &= 0.034\,[\pm0.007] + 0.862\,[\pm0.007]\,(u-b) \\ &\quad + 0.055\,[\pm0.006]\,(u-b)^2, \\ B - V &= -0.004\,[\pm0.004] + 1.039\,[\pm0.011]\,(b-v) \\ &\quad - 0.037\,[\pm0.007]\,(b-v)^2, \\ U - V &= 0.071\,[\pm0.010] + 0.899\,[\pm0.008]\,(u-v) \\ &\quad + 0.018\,[\pm0.003]\,(u-v)^2. \end{aligned}$$

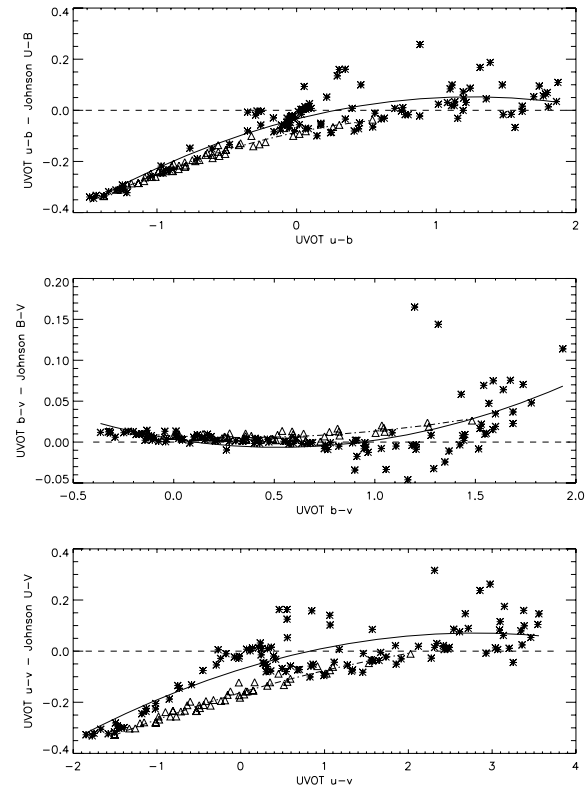

Figure 12. The differences between UVOT optical colours and Johnson optical colours for Pickles stars (stars) and GRB models (triangles): UVOT $u-b$ compared with Johnson $U-B$ versus UVOT $u-b$ (top plot); UVOT $b-v$ compared with Johnson $B-V$ versus UVOT $b-v$ (middle plot); and UVOT $u-v$ compared with Johnson $U-V$ versus UVOT $u-v$ (bottom plot). The solid lines represent the second-order polynomial fits to the Pickles stars, the dotted lines represent the second-order polynomial fit to the GRB models, and the dashed lines show where the colours in the two systems are equal. The polynomial fit parameters are given in Section 11.

The colour terms calculated from the second-order polynomial fits for the GRB models are

$$\begin{aligned} U - B &= 0.086\,[\pm0.003] + 0.886\,[\pm0.007]\,(u-b) \\ &\quad + 0.050\,[\pm0.006]\,(u-b)^2, \\ B - V &= -0.008\,[\pm0.001] + 1.012\,[\pm0.003]\,(b-v) \\ &\quad - 0.018\,[\pm0.002]\,(b-v)^2, \\ U - V &= 0.162\,[\pm0.002] + 0.904\,[\pm0.002]\,(u-v) \\ &\quad + 0.010\,[\pm0.002]\,(u-v)^2. \end{aligned}$$

Again, the ranges of colours over which the transforms were calculated are given in columns 5 and 6 of Table 7.

The observations of one faint white dwarf star and nine Landolt stars were then compared with these transforms. Observed count rates ($C_{\rm obs}$) were obtained using the method described in Section 6.4,

Table 7. rms error on residuals to colour fits. PS is Pickles star data fits and GRB is GRB model data fits. Columns 5 and 6 give the minimum and maximum limits on the *x*-axis (of Figs 12 and 14, respectively), which give the range of colours over which the transforms were calculated.

Fit	*y*-axis	*x*-axis	rms error	Minimum *x*-axis	Maximum *x*-axis
PS	$U-B$	$u-b$	0.057	−1.482	1.871
PS	$B-V$	$b-v$	0.025	−0.364	1.935
PS	$U-V$	$u-v$	0.075	−1.846	3.558
GRB	$U-B$	$u-b$	0.078	−1.380	0.543
GRB	$B-V$	$b-v$	0.034	−0.124	1.483
GRB	$U-V$	$u-v$	0.102	−1.505	2.026
PS	$B-b$	$b-v$	0.020	−0.364	1.935
PS	$B-b$	$u-b$	0.030	−1.482	1.871
PS	$V-v$	$b-v$	0.014	−0.364	1.935
PS	$V-v$	$u-v$	0.015	−1.846	3.558
PS	$U-u$	$u-b$	0.073	−1.482	1.871
PS	$U-u$	$u-v$	0.071	−1.846	3.558
GRB	$B-b$	$b-v$	0.001	−0.124	1.483
GRB	$B-b$	$u-b$	0.002	−1.380	0.543
GRB	$V-v$	$b-v$	0.004	−0.124	1.483
GRB	$V-v$	$u-v$	0.004	−1.505	2.026
GRB	$U-u$	$u-b$	0.011	−1.380	0.543
GRB	$U-u$	$u-v$	0.012	−1.505	2.026

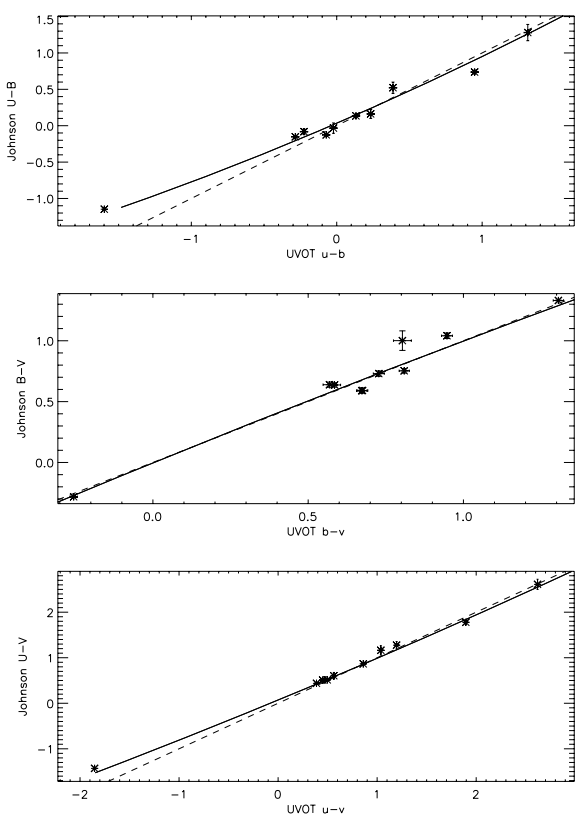

Figure 13. Johnson optical colours versus UVOT optical colours using observed data. The solid lines are the polynomial fit to the Pickles spectra shown in Fig. 12 and described in Section 11. The dashed lines show where the colours in the Johnson and UVOT systems are equal.

and converted into magnitudes using equation (7). Fig. 13 plots the Pickles star fits to the Johnson versus UVOT colours together with these observational data. The error bars on the observed data show the Poisson error in the raw observed count rate on the *x*-axis, and the errors associated with the Landolt colour terms in the *y*-axis (Landolt 1992). This figure shows that within the scatter of these observations, the fits produced with the Pickles stars agree with the observations.

Fig. 14 plots the difference between Johnson and UVOT magnitudes against UVOT colours. The stars in each plot represent the Pickles stars, whereas the triangles represent the GRB models. Fig. 14 shows that the Pickles spectra and GRB models follow different curves: the solid line in each plot shows the third-order polynomial fit to the Pickles stars, and the dashed line shows the second-order polynomial fit to the GRB models. The residuals to the fits are shown in the lower panel of each plot, and show good agreement within 0.05 mag, apart from a few outliers. As in Fig. 12, the outliers are due to Pickles spectra from stars with deep absorption features; we have included these in the plots to give the reader an idea of the appropriateness of the colour transformations for a range of star types. The rms error on the residuals can be seen in Table 7. The upper and lower colour limits for each colour transform are given in columns 5 and 6. The colour terms obtained from the Pickles polynomial fits are

$$\begin{aligned}
B-b &= 0.021\,[\pm0.003] + 0.005\,[\pm0.012]\,(b-v) \\
&\quad - 0.014\,[\pm0.022]\,(b-v)^2 - 0.011\,[\pm0.010]\,(b-v)^3, \\
B-b &= 0.011\,[\pm0.004] - 0.011\,[\pm0.008]\,(u-b) \\
&\quad - 0.008\,[\pm0.004]\,(u-b)^2 - 0.002\,[\pm0.004]\,(u-b)^3, \\
V-v &= 0.029\,[\pm0.002] - 0.009\,[\pm0.009]\,(b-v) \\
&\quad - 0.037\,[\pm0.016]\,(b-v)^2 + 0.017\,[\pm0.007]\,(b-v)^3, \\
V-v &= 0.026\,[\pm0.002] - 0.014\,[\pm0.002]\,(u-v) \\
&\quad - 0.005\,[\pm0.001]\,(u-v)^2 + 0.002\,[\pm0.0005]\,(u-v)^3, \\
U-u &= 0.042\,[\pm0.010] - 0.130\,[\pm0.020]\,(u-b) \\
&\quad + 0.053\,[\pm0.010]\,(u-b)^2 - 0.013\,[\pm0.010]\,(u-b)^3, \\
U-u &= 0.069\,[\pm0.012] - 0.093\,[\pm0.009]\,(u-v) \\
&\quad + 0.037\,[\pm0.007]\,(u-v)^2 - 0.007\,[\pm0.002]\,(u-v)^3.
\end{aligned}$$

The colour terms obtained for the GRB model fits are

$$\begin{aligned}
B-b &= 0.016\,[\pm0.0003] - 0.009\,[\pm0.001]\,(b-v) \\
&\quad - 0.023\,[\pm0.001]\,(b-v)^2, \\
B-b &= -0.018\,[\pm0.0005] - 0.045\,[\pm0.001]\,(u-b) \\
&\quad - 0.014\,[\pm0.001]\,(u-b)^2, \\
V-v &= 0.023\,[\pm0.001] - 0.021\,[\pm0.003]\,(b-v) \\
&\quad - 0.005\,[\pm0.003]\,(b-v)^2, \\
V-v &= 0.010\,[\pm0.0007] - 0.012\,[\pm0.0006]\,(u-v) \\
&\quad - 0.0009\,[\pm0.0006]\,(u-v)^2, \\
U-u &= 0.068\,[\pm0.003] - 0.159\,[\pm0.007]\,(b-b) \\
&\quad + 0.036\,[\pm0.006]\,(u-b)^2, \\
U-u &= 0.172\,[\pm0.002] - 0.108\,[\pm0.002]\,(u-v) \\
&\quad + 0.009\,[\pm0.002]\,(u-v)^2.
\end{aligned}$$

Fig. 15 plots the difference between the Johnson and UVOT magnitude versus UVOT colour for Pickles star fits in comparison with observed data. As before, the error bars on the observed data include the Poisson error in the raw observed count rate, and the errors associated with the Landolt colour terms (Landolt 1992).

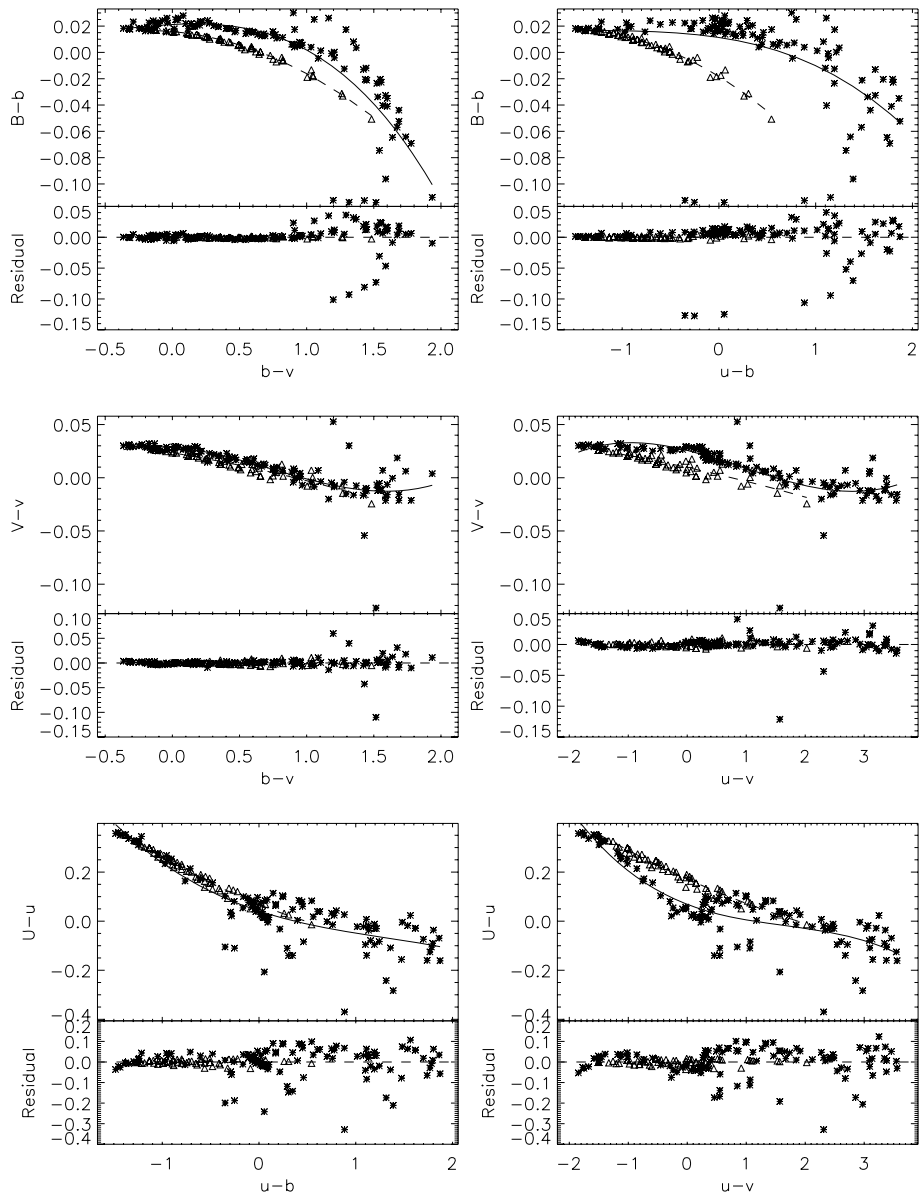

Figure 14. The difference between Johnson and UVOT magnitudes versus UVOT optical colours for Pickles spectra (stars) and GRB models (triangles): $B - b$ versus $b - v$ (top left-hand panel) and $u - b$ (top right-hand panel); $V - v$ versus $b - v$ (middle left-hand panel) and $u - v$ (middle right-hand panel); $U - u$ versus $u - b$ (bottom left-hand panel) and $u - v$ (bottom right-hand panel). The solid lines represent the third-order polynomial fits to the Pickles stars, and the dashed lines represent the second-order polynomial fits to the GRB models. The polynomial parameters are given in Section 11.

12 COUNT RATE TO FLUX CONVERSION

To compute an accurate flux density it is necessary to fold the source spectrum through the effective area curves. However, we have found for all but the *white* filter that there is not a strong dependency on stellar spectrum across a wide range of classes. Thus, in many cases an estimate of the flux can be obtained directly from the count rate and this can be particularly useful when plotting UVOT data with data from other instruments. Therefore a count rate to flux conversion factor has been calculated for each filter. Particular care should be taken where there may be significant absorption or emission features in the wavelength range of the filter (Table 1), and also with the conversion factor for the *white* filter, which depends strongly on spectral shape because of the wide wavelength range (1600–8000 Å).

The count rate to flux conversion for each filter was calculated, as described next, using Pickles spectra (Pickles 1998), and a subset of the GRB power-law spectral models described in Section 11 with redshifts in the range $0.3 < z < 1.0$.

The effective wavelength ($\lambda_{\rm eff}$) for each filter was calculated using the Vega spectrum (Bohlin & Gilliland 2004) in the following weighted formula:

$$\lambda_{\rm eff} = \frac{\int F_{\rm Vega}(\lambda) E_{\rm area}(\lambda) \lambda {\rm d}\lambda}{\int F_{\rm Vega}(\lambda) E_{\rm area}(\lambda) {\rm d}\lambda}, \quad (8)$$

where $F_{\rm Vega}(\lambda)$ is the Vega flux at a given wavelength, $\lambda, E_{\rm area}(\lambda)$ is the predicted effective area. The resultant effective wavelengths are shown in Table 8. It must be noted that tails of the UV filter transmission curves extend into the optical range, as shown in Fig. 2,

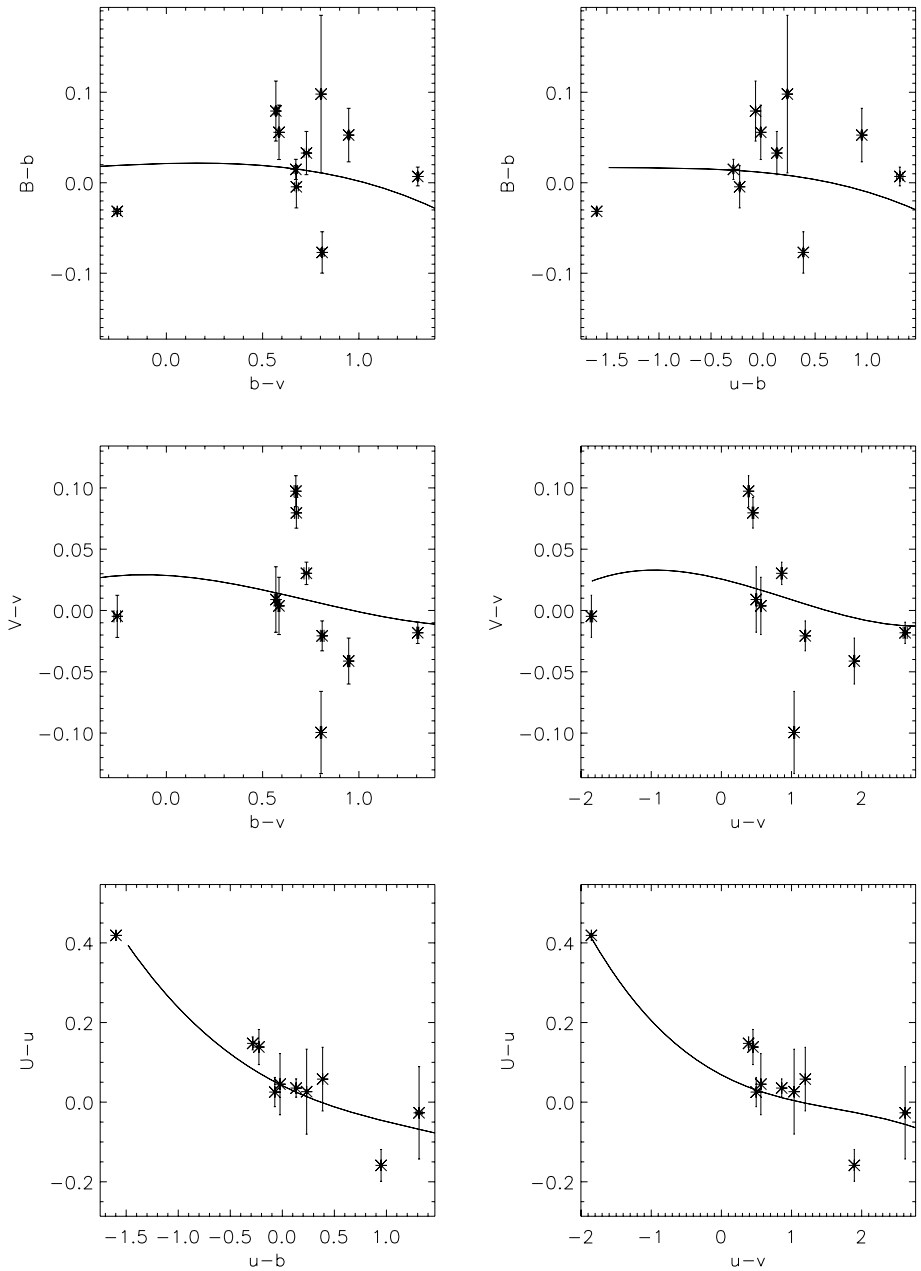

Figure 15. The difference between Johnson and UVOT magnitudes versus UVOT optical colours for observed data. The solid line shows for comparison the polynomial fit to the Pickles spectra illustrated in Fig. 14 and described in Section 11.

and thus the effective wavelengths for the UV filters for very red spectra will be longer than those given in Table 8.

A UVOT expected in-orbit count rate was calculated for each model spectrum in each filter by folding the spectrum through the UVOT in-orbit effective area curves (Section 9.2). A flux value at the effective wavelength for each model spectrum in each filter was obtained by smoothing the spectrum into 10 Å bins to remove narrow spectral features, and then interpolating over four points around the effective wavelength.

A count rate to flux conversion factor was then calculated for each spectrum and averaged to produce a count rate to flux factor for each filter. The average count rate to flux conversion factor for the Pickles star spectra and GRB models can be seen in Tables 9 and 10, respectively. The rms error (a measure of the data scatter) on the average factor is also given in each table, along with the range of UVOT $b - v$ colours over which the factors were calculated. Outside these ranges the conversion factors may not be applicable.

The large error in the *white* filter factor is due to large differences in the convolution of blue and red spectra with the *white* filter wavelength range. The *white* filter factor for Pickles spectra and GRB models across the UVOT colour $b - v$ and $uvw2 - v$ are shown in Figs 16 and 17, respectively, demonstrating the large scatter in the factor. In both figures the stars represent the Pickles stars and the triangles represent the GRB models.

13 VERIFICATION

We compared UVOT optical photometry measurements with photometry from other instruments in order to assess the accuracy of the UVOT photometric system independently. Three different groups

Table 8. Effective wavelengths for each filter, for a Vega-like spectrum, as calculated using equation (8).

Filter	Wavelength (Å)
v	5402
b	4329
u	3501
*uvw*1	2634
*uvm*2	2231
*uvw*2	2030
white	3471

Table 9. Average count rate to flux conversion factor results for the Pickles star spectra. The units on the conversion factor and errors are erg cm^{-2} s^{-1} Å^{-1}.

Filter	Conversion factor	rms	Minimum $b-v$ (mag)	Maximum $b-v$ (mag)
v	2.61×10^{-16}	2.4×10^{-18}	−0.36	1.09
b	1.32×10^{-16}	9.2×10^{-18}	−0.36	1.09
u	1.5×10^{-16}	1.4×10^{-17}	−0.36	1.09
*uvw*1	4.3×10^{-16}	2.1×10^{-17}	−0.36	0.1
*uvm*2	7.5×10^{-16}	1.1×10^{-16}	−0.36	0.1
*uvw*2	6.0×10^{-16}	6.4×10^{-17}	−0.36	0.1
white	2.7×10^{-17}	7.9×10^{-18}	−0.36	1.09

Table 10. Average count rate to flux conversion factor results for GRB models. The units on the conversion factors and errors are erg cm^{-2} s^{-1} Å^{-1}.

Filter	Conversion factor	rms	Minimum $b-v$	Maximum $b-v$
v	2.614×10^{-16}	8.7×10^{-19}	−0.12	0.73
b	1.472×10^{-16}	5.7×10^{-19}	−0.12	0.73
u	1.63×10^{-16}	2.5×10^{-18}	−0.12	0.73
*uvw*1	4.00×10^{-16}	9.7×10^{-18}	−0.12	0.03
*uvm*2	8.50×10^{-16}	5.6×10^{-18}	−0.12	0.03
*uvw*2	6.2×10^{-16}	1.4×10^{-17}	−0.12	0.03
white	3.7×10^{-17}	4.9×10^{-18}	−0.12	0.73

working independently performed the comparison using different data, and using software other than that used for the calibration work. The software used included the latest HEASOFT *Swift* uvotsource program in one case, and a combination of the uvotdetect and uvotmag (whose functionality has since been taken over by uvotflux) programs in another, while a test version of the CalDB incorporating the new calibration was employed.

The tests directly compared measured optical magnitudes with those published in the literature. The sources used for u, b and v were: two sets of observations of 23 stars in the GRB051021a field and 36 stars in the GRB051022 field (from Henden ftp://ftp.aasvo.org/public/grb); 10 stars in the field of the SN2005am (as calibrated by Li et al. 2006); six sources in the GRB060218 field (calibrated by Hicken et al. 2006). In addition the photometry of stars in the field PG1633+099B have been compared with magnitudes given by Stetson (2000); this work is shown in Section 1.4.1.

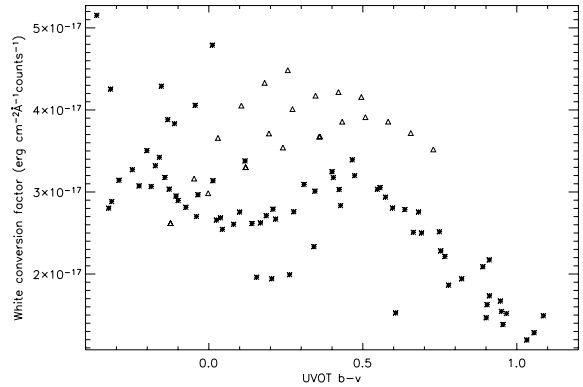

Figure 16. This plot shows how the *white* filter count rate to flux conversion factor varies with $b-v$ UVOT colours. The stars represent the Pickles data, and the triangles represent the GRB model data.

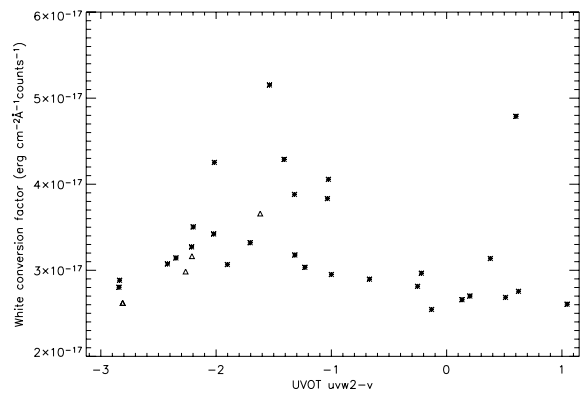

Figure 17. This plot shows how the *white* filter count rate to flux conversion factor varies with $uvw2-v$ UVOT colours. The stars represent the Pickles data, and the triangles represent the GRB model data.

Not all the measurements were made in the central region where the throughput is most uniform (see Section 8). Those in the GRB060218 and SN2005am fields were distributed fairly randomly across the detector in individual exposures. For the GRB051021a and GRB051022 fields, about half the stars fell outside the central four squares in Fig. 8, but did not fall in the corners; the LSS for the positions of the majority of these sources is estimated to vary from 0.99 to 1.02.

The u, b and v magnitudes were obtained from UVOT observations using the HEASOFT tools mentioned above. After converting these instrumental magnitudes into Johnson U, B and V magnitudes using the colour corrections (equations in Section 11), comparisons were made with published U, B, V photometry.

In general, the differences in magnitudes as observed by UVOT and those obtained from references as described above are small (see Table 11). There is no evidence for a bias in any of the magnitude differences. The transformed UVOT colours $(b-v)_{\rm trans}$ and $(u-b)_{\rm trans}$ also match well with the reference samples.

13.1 Binned data

The photometric calibration of the UVOT is based upon data taken in 1 × 1 binned (i.e. unbinned) modes. However, a large fraction of observations by the UVOT are made using 2 × 2 binned modes, to reduce the telemetry volume generated onboard the spacecraft. We

Table 11. Comparisons of UVOT measurements of optical magnitudes with literature magnitudes. The UVOT optical magnitudes and colours have been transformed to the Johnson system using the colour transformations.

Magnitude UVOT − other	Mean difference (mag)	rms error	No. of sources	No. of data sets
$v_{\rm trans} - V$	0.019	0.020	81	5
$b_{\rm trans} - B$	−0.024	0.016	81	5
$u_{\rm trans} - U$	−0.036	0.036	65	4
$(b - v)_{\rm trans} - (B - V)$	−0.028	0.004	59	2
$(u - b)_{\rm trans}$ − (U–B)	0.024	0.007	59	2

have checked whether the binning mode has a significant effect on the photometric calibration, by comparing the count rates of a set of stars observed in 1 × 1 and 2 × 2 binned modes. The average difference in the count rates for 30 stars in the field of GRB060206, in the UVOT v band using a 5 arcsec radius aperture (5 pixels for the 2 × 2 binning), is less than 1 per cent of the average count rate, which is less than the average measurement error based on Poisson statistics. We conclude that there is no evidence for a significant difference in the count rates measured in 1 × 1 and 2 × 2 binned modes. Thus this calibration should be relevant to 2 × 2 binned and unbinned data.

14 PRACTICAL PHOTOMETRY

The data analysis described earlier, in Section 6, concerned the method used to obtain an optimal calibration over a broad range of source strengths. If the reader were to follow this method (using a 5 arcsec aperture and a large source-free background annulus more than 27 arcsec from the source), they should obtain reasonable results.

However, when doing photometry on point sources, particularly faint ones, the size and shape of the extraction aperture needs to be optimized to take into account the size and shape of the PSF, the degree of crowding in the exposure, and the desired science. For isolated point sources the optimal aperture should maximize the signal-to-noise ratio. We have found that in most cases the maximum signal-to-noise ratio is obtained with an aperture radius between 2.5 and 4 arcsec, but the actual value depends on the strength of the source, the density of sources in the field and the background level. Li et al. (2006) similarly found an optimum aperture radius of 2.5 arcsec for unbinned UVOT data and 3 arcsec for binned data for the fields they were working with. Their work focused on comparing UVOT optical photometry with standard fields, and their calibration is based directly on these apertures.

Since the UVOT calibration is based on counts measured within a 5 arcsec aperture, a correction must be made if a different aperture is used. The size of the correction depends on the PSF of the source of interest which in turn depends on the filter being used. The PSF is also observed to vary slightly throughout the orbit as the instrument changes temperature. The CalDB contains a set of 'average' PSFs for each filter which can be used to derive a correction; an 'average' magnitude correction has been derived and included in Table 12 for quick reference. The HEASOFT *Swift* software tools uvotsource and uvotapercorr use these PSFs to derive corrections for any specified user aperture. However, if this method is to be used, we caution against using an aperture smaller than 3 arcsec because the orbital variations in the PSF have a significant influence on photometry calculated with smaller apertures.

Table 12. Aperture corrections are given here in terms of magnitude for apertures having radii from 2 to 4.5 arcsec, calculated with the uvotapercorr task Swift_Rel2.7(Bld21)_15Jun2007, using the CalDB file swureef20041120v102.fits. The 2.0 or 2.5 arcsec aperture radii are not generally recommended, for reasons given in Section 14, but may be the best option where the field is very crowded or the background is complex.

Aperture (arcsec)	2.0	2.5	3.0	3.5	4.0	4.5
v	−0.276	−0.145	−0.091	−0.054	−0.032	−0.014
b	−0.327	−0.176	−0.111	−0.065	−0.037	−0.015
u	−0.329	−0.169	−0.103	−0.059	−0.034	−0.015
$uvw1$	−0.405	−0.212	−0.126	−0.069	−0.037	−0.015
$uvm2$	−0.342	−0.182	−0.109	−0.060	−0.033	−0.014
$uvw2$	−0.417	−0.222	−0.133	−0.073	−0.039	−0.016
white (b)	−0.327	−0.176	−0.111	−0.065	−0.037	−0.015

An alternative method that eliminates the problem of the small orbital variation is to derive the aperture correction on an exposure by exposure basis. This also automatically copes with the PSF filter dependency. Furthermore, during settling exposures, or very occasionally when there are attitude problems, the pointing can drift during the exposure, causing the images to be blurred. In these cases an exposure-specific correction is essential. The shape of the UVOT PSF also depends on the count rate of the source; bright sources ($\geqslant$10 counts s^{-1}) have narrower PSFs than faint ones because of coincidence loss effects. This count rate PSF variation could be compensated for by deriving separate aperture corrections for sources with different count rates. In practice both the orbital variation and count rate dependency changes the aperture correction by only a few per cent, except for very high count rates, in which case a small aperture is not appropriate.

We present here a suggested method for obtaining well calibrated data from UVOT, using a small aperture plus an exposure-specific aperture correction, and include an example of this method below. However, we do not wish to be overly prescriptive, or to tie the user to any particular software tools. The reader should not be afraid to experiment with different apertures or background regions for different situations.

One method of aperture correcting for each exposure is as follows.

(i) Identify a set of 5–15 isolated stars in the exposure. These stars should be bright enough that there is signal in the wings of the PSF, but not so bright that coincidence loss is distorting the PSF (i.e. between a few and about 10 counts s^{-1}). There should be no neighbouring sources detectable within at least 10 arcsec to avoid using stars that are contaminated by light from other sources.

(ii) Perform photometry on each of these stars with both the user-supplied aperture and the 5 arcsec standard photometric aperture.

(iii) Subtract the magnitudes in the user-supplied aperture from the magnitudes in the 5 arcsec aperture to get the aperture corrections.

(iv) The mean of the 5–15 aperture corrections thus obtained can then be used as the aperture correction for that exposure. To estimate the error in the aperture correction, it takes the rms of the individual values about the mean value.

(v) The aperture correction is added to the magnitudes of the sources of interest measured in the user-supplied aperture in the same exposure.

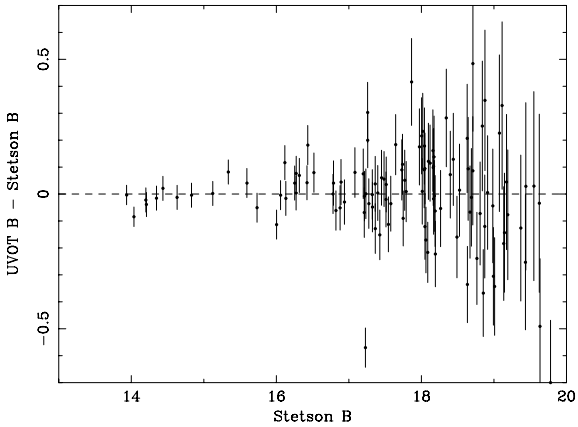

Figure 18. A comparison of magnitudes from UVOT data of the PG1633+099B field, obtained using the exposure-specific aperture correction method outlined in Section 14, with those from Stetson (2000).

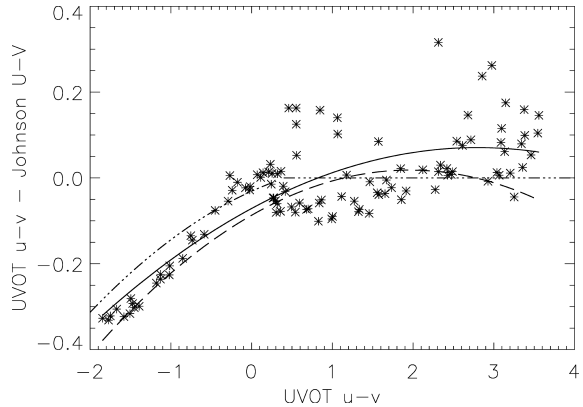

Figure 19. UVOT $u - v$ compared with Johnson $U - V$ for Pickles stars (stars) as plotted in Fig. 12. The solid line represents the second-order polynomial fit to the Pickles stars given in Section 11, the dashed line represents the fit given in the initial calibration (CalDB released 20050805). The transformation given by Li et al. (2006) is shown by the dash–dotted line.

The error in the aperture correction factor for a single measurement is not simply the square root sum of the measurements at the chosen and the standard aperture. That is because the photons in the smaller aperture are counted in measurements with both apertures. It can be shown that the error in the aperture correction factor is the measurement error in the largest aperture. It is useful to use this error for deriving the weighted average from multiple measurements, especially if the stellar magnitudes of the reference stars vary.

14.1 Using an aperture correction

The stars in the PG1633+099B field have been analysed and calibrated using the exposure-specific method outlined above. The results (shown in Fig. 18) can be compared directly with Stetson's photometry giving confidence that the method works well. The mean offset between Stetson and UVOT photometry in this data set is <0.01 mag, with a standard deviation of 0.06 mag for stars brighter than 17th magnitude, and 0.18 mag if all the stars are included.

We tested the simple standard PSF approach as used by the uvotapercorr tool in comparison with the exposure-specific method described above. The comparison was done for two v-filter data sets. We used uvotsource (which calls uvotapercorr) to perform photometry on several isolated stars in each frame using both 3 and 5 arcsec circular apertures. An aperture correction to convert from 3 to 5 arcsec magnitudes was computed for each frame and compared to the aperture correction derived from the v filter PSF given in the CalDB. We found that the aperture correction derived from the PSF for these two fields underestimated the brightness of the point sources by 0.020 mag in the 00055751001 exposures and 0.019 mag in the 00276321001 exposures. These examples confirm the fact that the aperture corrections derived from the PSFs are reliable to a precision of a few hundredths of a magnitude, but that aperture corrections specific to each exposure need to be computed if high-precision photometry is desired. Similar offsets are found for different combinations of filter and aperture size.

15 DISCUSSION

The approach we have taken in this work is superior in a number of ways to that which was used to produce the initial in-orbit UVOT photometric calibration (Breeveld et al. 2005). A full description of the earlier calibration is beyond the scope of this paper, but we note here three particularly significant improvements.

(i) The shape of the instrument response curve used in this work, which is based on measurements of the individual UVOT optical elements, is a much closer representation of the true instrument response than that used for the original calibration, which, although it was a direct measurement and consistent with the current instrument response, was not of high precision, and was sparsely sampled in wavelength.

(ii) The effective areas and zero-points are determined for the same aperture for all filters (5 arcsec radius), that is optimized to minimize the enclosed-energy dependence on coincidence loss and hence count rate. In our initial calibration the effective areas and zero-points were based on different (and less-optimum) apertures for the UV and optical filters.

(iii) The zero-points for optical and UV filters are generated using a single procedure in the new calibration, whereas in the initial calibration the optical zero-points were obtained such that the mean difference was zero between UVOT and Johnson magnitudes of a group of standard stars: in effect calibrating the UVOT as though its optical filters had a response identical to the Johnson system. Defining a UVOT-based magnitude system, and then facilitating conversion to the Johnson system using colour transformations gives an inherently more accurate, stable and understandable calibration.

For comparison with previously released colour transformations the $U - V$ to $u - v$ fit for Pickles stars (as shown in the bottom panel of Fig. 12) has been plotted again in Fig. 19, but this time we have added the initial in-orbit calibration from CalDB 20050805 (dashed line) and also the colour correction provided in Li et al. (2006) (dash–dotted line). Li et al. (2006) suggest no colour correction for the v and b filters, which would therefore be represented by the dashed horizontal line in the middle panel of Fig. 12. The GRB models and fit are not included in this comparison plot because this is the first time colour transformations have been provided for GRBs.

For a full list of changes to the calibration approach, procedures and observations, the reader is referred to the calibration documentation on the *Swift* web site. The CalDB documentation and files containing the calibrations presented in this paper are available from the HEASARC CalDB at http://swift.gsfc.nasa.gov/

docs/heasarc/caldb/swift/ in version 20070627 of the Swift/UVOTA CalDB. In the event that the reader wishes to compare new results with data processed with previous versions of the pipeline or calibration products, they are advised to reprocess the older data. The pipeline has been revised to take care of exposure time problems and to flag any remaining problems.

15.1 Future photometric calibration

Although we consider the photometric calibration of UVOT as presented here to be in good shape, there are a number of areas in which we are working to further improve and refine the calibration. For example, we plan to measure the sensitivity variation over the detector with a higher spatial resolution than was possible using the observations described in Section 8. For this purpose, we have made a sequence of 55 observations of a dense star field (more than 300 stars) at a range of offsets and orientations, so that each individual star is observed at least 30 times, each at different locations on the detector. The high density of data across the detector and large number of stars will allow us to model the detector response spatially to minimize photometric error. The goal is to use these observations to construct a flat-field calibration product which will enable us to achieve a photometric response that is uniform to 1–2 per cent over the entire detector area.

It would be desirable to increase the number of standard stars and the colour range on which the UV and *white* filters are calibrated. The main limitation is the lack of UV spectrophotometric standard stars which are sufficiently faint for UVOT. This may be overcome in two ways: by using smaller hardware windows we can bring some brighter standards within the range of calibrated coincidence loss, and also we would like to make use of white dwarfs from the Sloan Digital Sky Survey (Ivezic et al. 2007) for which there are accurate models of the UV flux.

We also plan to characterize the PSF out to a large radius to enable, for example, reliable surface photometry.

The detector response is expected to decline gradually with total radiation dose. From experience with *XMM*-OM we expect this to be at a level of 1–2 per cent per year. Although this decline is not yet large enough to be measured, continued observations of standard stars will allow us to measure and calibrate the changing photometric response of UVOT.

There is also more work to be done on various aspects of practical photometry, for instance, by developing an optimal sky-fitting algorithm to remove stars in the background region, given that the background is usually in the Poisson statistics regime rather than the normally assumed Gaussian. Also, the parameterization of the PSF with count rate and with orbital variations will lead to the development of more accurate aperture corrections.

15.2 Summary

In this paper we have presented the in-orbit photometric calibration of the UVOT and defined the UVOT photometric system. We have discussed factors which affect the accuracy of the photometry. Any observational science depends critically on the calibration of the instruments; the UVOT calibration is itself based on trusted sources and data processed with the most up-to-date software. The comparison with other calibrated data sets gives us confidence that we have a robust, reliable and accurate system.

ACKNOWLEDGMENTS

We would like to thank Weidong Li, Joshua Bloom and Alexei Filippenko for testing the calibration and for useful discussions. *Swift* UVOT was designed and built in collaboration between MSSL, PSU, SwRI, Swales Aerospace and GSFC, and was launched by NASA. We would like to thank all those involved in the continued operation of UVOT at PSU, MSSL and GSFC, and those involved in the data processing and the writing of analysis software. This work is supported at MSSL by funding from PPARC and at PSU by NASA's Office of Space Science through grant NAS5-00136. Some of the standard spectra used in this paper were obtained from the Multimission Archive at the Space Telescope Science Institute (MAST). STSci is operated by the Association of Universities for Research in Astronomy, Inc., under NASA contract NAS5-26555. Support for MAST for non-*HST* data is provided by the NASA Office of Space Science via grant NAG5-7584 and by other grants and contracts. We acknowledge the use of public data from the *Swift* data archive.

REFERENCES

Ažusienis A., Straižys, V., 1969, SvA, 13, 316
Barthelmy S. D. et al., 2005, Space Sci. Rev., 120, 143
Bessel M. S., 2005, Annu. Rev. Astron. Astrophys., 43, 293
Bianchi L., 2000, Mem. Soc. Astron. Ital., 71, 1117
Blackburn J. K., 1995, in Shaw R. A., Payne H. E., Hayes J. J. E. eds, ASP Conf. Ser. Vol.77, Astronomical Data Analysis Software and Systems IV. Astron. Soc. Pac., San Francisco, p. 367
Bohlin R. C., 2007, in Sterken C., ed., ASP Conf. Ser. Vol. 364, The Future of Photometric Spectrophotometric and Polarimetric Standardization. Astron. Soc. Pac., San Francisco, p. 315
Bohlin R. C., Gilliland R. L., 2004, AJ, 127, 3508
Breeveld A. A. et al., 2005, Proc. SPIE, 5898, 391
Burrows C. J., 1994, *Hubble Space Telescope* Wide Field and Planetary Camera 2 Instrument Handbook, Vol. 2. Space Telescope Science Institute, Baltimore, MD
Burrows D. N. et al., 2005, Space Sci. Rev., 120, 165
Buser R., 1978, A&A, 62, 411
Colina L., Bohlin R. C., 1994, AJ, 108, 1931
Fordham J. L. A., Bone D. A., Oldfield M. K., Bellis J. G., Norton T. J., 1992, in Guyenne T. D., Hunt J. J., eds, ESA SP-356, Proc. ESA Symp. Photon Detectors for Space Instrumentation ESA Publications Division, Noordwijk, p. 103
Fordham J. L. A., Moorhead C. F., Galbraith R. F., 2000, MNRAS, 312, 83
Gehrels N. et al., 2004, ApJ, 611, 1005
Hicken M., Modjaz M., Challis P., Kirshner R., Prieto J. L., Stanek K., Cool R., 2006, GCN, 4898, 1
Holberg J. B., Barstow M. A., Burleigh M. R., 2003, ApJS, 147, 145
Ivanushkina M. et al., 2005, Proc. SPIE, 5898, 371
Ivezic Z., Allyn Smith J., Miknaitis G., Lin H T. D., 2007, AJ, 34, 973
Kawakami H., 1999, XMM-OM/MSSL/TC/0053.01, Table 3
Kawakami H., Bone D., Fordham J., Michel R., 1994, Nucl. Instrum. Methods Phys. Res. A, 348, 707
Kuin N. P. M., Rosen S. R., 2007, preprint (arXiv:0709.1208)
Landolt A. U., 1992, AJ, 104, 340
Li W., Jha S., Filippenko A. V., Bloom J. S., Pooley D., Foley R. J., Perley D. A., 2006, PASP, 118, 37
Mason K. O. et al., 2001, A&A, 365, L36
Massa D., Fitzpatric E. L., 2000, ApJS, 126, 517
Massey P., Strobel K., Barnes J. V., Anderson E., 1988, ApJ, 328, 315
Menzies J. W., Marang F., Laing J. D., Coulson I. M., Engelbrek L. A., 1991, MNRAS, 248, 642
Michel R., Fordham J., Kawakami H., 1997, MNRAS, 292, 611

Milliard B. et al., 2001, in Banday A. J., Zaroubi S., Bartelmann M., eds, ESO Astrophysics Symp., Mining the Sky: Proc. MPA/ESO/MPE Workshop. Springer-Verlag, Berlin, p. 201
Pei Y. C., 1992, ApJ, 395, 130
Pickles A. J., 1998, PASP, 110, 863
Pogson N., 1856, MNRAS, 17, 12
Poole T. S., 2007a, SWIFT-UVOT-CALDB-05-R02
Poole T. S., 2007b, SWIFT-UVOT-CALDB-01-R03
Poole T. S., 2007c, SWIFT-UVOT-CALDB-03-R02
Roming P., 2003, PSU Document no. SWIFT-UVOT-204-R01, Swift UVOT Instrument Science Report – Effective Area
Roming P., 2007, PSU Document no. SWIFT-UVOT-400-R01, Swift UVOT Instrument Science Report – Mirror Reflectivity
Roming P. W. A. et al., 2005, Space Sci. Rev., 120, 95
Siegmund O. H. W. et al., 2004, Proc. SPIE, 5488, 13
Stetson P. B., 2000, PASP, 112, 925
Stetson P. B., McClure R. D., VandenBerg D. A., 2004, PASP, 116, 1012

This paper has been typeset from a TEX/LATEX file prepared by the author.